Marine Chemistry 258 (2024) 104346

Contents lists available at ScienceDirect

Marine Chemistry

journal homepage: www.elsevier.com/locate/marchem

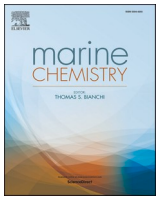

Carbon and silica fluxes during a declining North Atlantic spring bloom as part of the EXPORTS program

Samantha J. Clevenger [a], Claudia R. Benitez-Nelson [b], Montserrat Roca-Martí [c,d,e], Wokil Bam [c], Margaret Estapa [f], Jennifer A. Kenyon [a], Steven Pike [c], Laure Resplandy [g], Abigale Wyatt [g], Ken O. Buesseler [c,*]

[a] MIT-WHOI Joint Program in Oceanography, Applied Ocean Science and Engineering, Cambridge, MA, United States
[b] School of the Earth, Ocean and Environment, University of South Carolina, Columbia, SC, United States
[c] Department of Marine Chemistry and Geochemistry, Woods Hole Oceanographic Institution, Woods Hole, MA, United States
[d] Department of Oceanography, Dalhousie University, Halifax, Nova Scotia, Canada
[e] Institut de Ciència i Tecnologia Ambientals (ICTA-UAB), Universitat Autònoma de Barcelona, 08193 Cerdanyola del Vallès, Barcelona, Spain
[f] Darling Marine Center, School of Marine Sciences, University of Maine, Walpole, ME, United States
[g] Department of Geosciences, Princeton University, Princeton, NJ, United States

ARTICLE INFO

Keywords:
Biological carbon pump
Carbon export
Thorium
Radionuclides
North Atlantic Ocean spring bloom
Diatom bloom
Biogenic silica export
Porcupine Abyssal Plain

ABSTRACT

The goal of NASA's EXport Processes in the Ocean from RemoTe Sensing (EXPORTS) project is to develop a predictive understanding of the fate of global ocean primary productivity and export of carbon from the surface to the deep ocean. Thorium-234 (^{234}Th, $t_{1/2}$ = 24.1 d) was used to measure sinking particle export from an anticyclonic eddy during the EXPORTS North Atlantic cruise (May 2021) at the Porcupine Abyssal Plain. The four-week sampling period was broken into three time periods ("epochs") where 800 ^{234}Th seawater samples were collected from over 50 CTD casts with high depth resolution over the upper 500 m. Size-fractioned particulate samples were collected to determine particulate organic carbon (POC) and biogenic silica (bSi) to ^{234}Th ratios using in situ McLane pumps. A ^{234}Th non-steady state model shows an eddy center epoch average progression of increasing ^{234}Th export (~2800 ± 300 (Epoch 1; standard deviation) to 4500 ± 700 (Epoch 3) dpm m^{-2} d^{-1}) out of the top 110 m of the water column over the course of the cruise (29 d). This translates into an epoch average progression of ~11 ± 1 to 14 ± 2 mmol C m^{-2} d^{-1} of sinking POC flux, and ~ 3 ± 1 to 6 ± 1 mmol bSi m^{-2} d^{-1} of sinking bSi flux to deeper waters at 110 m. The overall efficiency of the biological carbon pump (amount of net primary production reaching 100 m below the euphotic zone) increases from ~10% to ~30% throughout the sampling period. The temporal trends discussed extensively in this paper show that POC and bSi export increase during diatom bloom evolution.

1. Introduction

The biological carbon pump (BCP) is an important component of the natural global carbon cycle, as it helps control and regulate carbon dioxide (CO_2) uptake from the atmosphere into the ocean. It is estimated that the ocean acts as a sink for up to one-third of global anthropogenically emitted CO_2 (Friedlingstein et al., 2022), with approximately 1% ultimately reaching the seafloor on average (Feely et al., 2001). The processes controlling the magnitude of sequestration and burial canonically include both the BCP and the solubility pump (Volk and Hoffert, 1985; McKinley et al., 2016). While the solubility pump mostly transfers cold, dissolved inorganic carbon-rich water to depth at high latitudes, the BCP is responsible for export of particulate organic carbon (POC) to depth, largely via gravitational settling referred to as the biological gravitational pump (BGP) (Sarmiento and Gruber, 2006; Buesseler et al., 2007; Boyd et al., 2019). More recently, active injection of particles to depth via physical mediation (e.g., subduction) or biological mediation (e.g., diel vertical migration) has been considered as an additional pathway of carbon sequestration and burial, termed the particle injection pump (PIP) (Lévy et al., 2013; Omand et al., 2015; Jónasdóttir et al., 2015; Dall'Olmo et al., 2016; Stukel et al., 2017; Boyd et al., 2019). Despite the seemingly small total burial of ~1%, atmospheric CO_2

* Corresponding author at: Woods Hole Oceanographic Institution, Mail Stop 25, 266 Woods Hole Rd, Woods Hole, MA, United States.
E-mail address: kbuesseler@whoi.edu (K.O. Buesseler).

https://doi.org/10.1016/j.marchem.2023.104346
Received 27 May 2023; Received in revised form 23 November 2023; Accepted 3 December 2023
Available online 12 December 2023

relative to preindustrial levels would be ~50% higher than it is now if not for the current strength of the BCP (Sarmiento and Toggweiler, 1984; Parekh et al., 2006; Sanders et al., 2014). In the total absence of the BCP-mediated BGP, models predict that atmospheric CO_2 could be nearly twice as high (Maier-Reimer et al., 1996). Even subtle changes in the magnitude of the BCP and the depth of remineralization – and therefore the magnitude of the downward transport of carbon from the surface to the deep ocean – can have a large impact on global CO_2 levels (Kwon et al., 2009). The North Atlantic in particular is believed to be a critical component of the global BCP due to its extensive productivity and bloom dynamics (e.g., Buesseler et al., 1992; Robertson et al., 1993; Alkire et al., 2012; Henson et al., 2019). Thus, the study of the North Atlantic BCP system is crucial to understanding the current state of the global carbon cycle and its future changes. Here, we use the radioactive isotope thorium-234 (^{234}Th, $t_{1/2}$ = 24.1 d) to quantify the downward flux of POC and biogenic silica (bSi) associated with sinking particles throughout an anticyclonic eddy during the North Atlantic bloom, as part of NASA's EXport Processes in the Ocean from RemoTe Sensing (EXPORTS) program.

The spring bloom in the Northeast Atlantic Ocean is an annually recurrent event, hypothesized to be initiated by three main factors: (1) the critical depth hypothesis wherein springtime stratification of the upper ocean shoals the mixed layer (Savidge et al., 1995; Bury et al., 2001; Henson et al., 2009; Martin et al., 2011), thereby fueling production that exceeds loss (Riley, 1942; Sverdrup, 1953); (2) critical turbulence hypothesis wherein a bloom is initiated in an arbitrarily deep layer with changes in mixing intensity (Huisman et al., 1999), and; (3) the dilution-recoupling hypothesis wherein decreasing grazing pressure controls the bloom onset (Behrenfeld, 2010; Behrenfeld et al., 2013). Reviews of these three hypotheses at our study site, Porcupine Abyssal Plain (PAP), can be found in Rumyantseva et al. (2019) and Binetti et al. (2020), both showing that the critical depth hypothesis is most responsible for bloom initiation. In the North Atlantic Ocean, production is at first dominated by fast-growing diatoms and coccolithophores, until surface silicate is depleted, at which point the system shifts to smaller flagellates and picophytoplankton (Lochte et al., 1993; Sieracki et al., 1993; Leblanc et al., 2009). Our study site, PAP, is considered representative of the overall open ocean within the North Atlantic Drifting Province (Longhurst, 1991), and the PAP Sustained Observatory has produced much of our contemporary understanding of temporal variation in the deep sea, as well as links between the surface ocean and seabed, over the past three decades (Hartman et al., 2021). Prior studies have shown that during the sampling time period at the late stages of the spring bloom, the PAP site is dominated by diatoms and haptophytes, although the overall phytoplankton community during the spring bloom is highly dynamic (Leblanc et al., 2009; Smythe-Wright et al., 2010). Much of the organic carbon at PAP is exported as large, fast sinking particles accessible to large zooplankton, although prokaryotes are estimated to be responsible for 70 to 92% of estimated remineralization below the surface (~50 m) (Giering et al., 2014). Consideration of community composition to understand surface carbon export efficiency is important, as export is highly variable depending on the coupling of primary producers and upper ocean remineralization by zooplankton and bacteria (Henson et al., 2019; Koski et al., 2020). Indeed, at PAP biological productivity and temperature account for about 77% of the annual change in pCO_2 (Macovei et al., 2020). These biological dynamics have been shown in prior studies to lead to high export efficiencies, with an Ez-ratio ($Flux_{Ez}$/NPP) ranging from 0.2 to 0.4, and flux transmission to 100 m below the euphotic zone ($Flux_{Ez+100}/Flux_{Ez}$) ranging from 0.5 - > 1.0, where NPP is net primary productivity, Ez is the depth of the euphotic or sunlit zone of the ocean, and the $Flux_{Ez}$ is flux at the Ez (Buesseler and Boyd, 2009; Buesseler et al., 2020a).

The ^{234}Th approach to measuring particle export is based upon the disequilibrium between the particle-reactive ^{234}Th and its soluble, naturally occurring radioactive parent uranium-238 (^{238}U, $t_{1/2}$ = $4.47{\cdot}10^9$ y) in seawater. In oxygenated seawater, ^{238}U exists predominantly in the dissolved form as $UO_2(CO_3)_3^{4-}$ and is conservatively distributed throughout the water column with respect to salinity (Langmuir, 1978; Santschi et al., 2006; Owen et al., 2011). Given their half-lives, if there were no particles in the ocean, ^{238}U and ^{234}Th would be in secular equilibrium in seawater (i.e., their activities would be equal). However, when particles are present, primarily through biological activity, ^{234}Th is rapidly scavenged. When those particles sink, they remove ^{234}Th from the water column causing disequilibrium with ^{238}U. The net deficit of ^{234}Th can therefore be used to measure the flux of ^{234}Th on passively sinking particles (i.e., biogenic material) out of a given ocean depth (e.g., Cochran and Masqué, 2003; Verdeny et al., 2009). Studies using ^{234}Th to determine POC flux have been carried out since the early 1990's (seminally in Buesseler et al., 1992) following initial studies focusing exclusively on rates of particle cycling beginning in the 1960's (e.g., Bhat et al., 1969; Li et al., 1979; Kaufman et al., 1981; Bacon and Anderson, 1982; Bacon et al., 1985; Coale and Bruland, 1987; Nozaki et al., 1987; Huh et al., 1989). Thorium-234 use has more recently been extended to allow for flux analyses of other species beyond POC, including pollutants, metals, and bioelements (e.g., Gustafsson et al., 1997; Weinstein and Moran, 2005; Black et al., 2018; Black et al., 2020; Tesán Onrubia et al., 2020; Roca-Martí et al., 2021).

2. Study overview and analysis context

Samples were collected during the EXPORTS 2021 field campaign in the vicinity of the PAP site (approximately 48.5°N, 16.3°W) in the larger context of a North Atlantic spring bloom. This served as the "strong" BCP endmember compared to the EXPORTS 2018 campaign in the North Pacific Ocean Station Papa (OSP) site (Siegel et al., 2016; Buesseler et al., 2020b). Sampling followed an anticyclonic eddy during late spring 2021, capturing a transition in the spring bloom. The goal of following a Lagrangian (i.e., retentive) eddy, as opposed to random sampling of an eddy field, was to capture a time series-style analysis of the biological and chemical dynamics – and ultimately carbon export – occurring in an eddy. Details on finding and tracking a strong, retentive eddy for this field study can be found in Erikson et al., 2022. Samples were classified as coming from the eddy center (EC, < 15 km from autonomous asset-defined eddy center, see diamonds in Fig. 1) and non-eddy center (NEC, > 15 km from eddy center, see circles in Fig. 1). Data will be presented in the context of these two groups. A 15 km radius was identified by Johnson et al. (2024) as the radius wherein 86% of casts taken had a stable and consistent temperature and salinity regime, and is therefore what the majority of the EXPORTS program considers the eddy center in analysis.

Extensive sampling of ^{234}Th occurred on the *RRS Discovery* (DY131; 01–29 May; hereafter referred to in text as the "Survey" ship or data), both in and outside of the eddy center and on the edges of the eddy (Fig. 1). The Survey cruise took place as part of a three-ship operation, also including the *RRS James Cook* (JC214; NASA EXPORTS; 04–29 May; hereafter referred to as the "Process" ship), and the *R/V Sarmiento de Gamboa* (SG2105; WHOI Ocean Twilight Zone Project; 05–19 May; hereafter referred to as the "Trophic" ship). The Process ship sampled exclusively within the EC, while the Trophic ship sampled a wider survey of the eddy (both EC and NEC locations) similar to the Survey ship.

The EXPORTS 2021 field study was broken into three "epochs," with sampling dates of: 04–10 May (Epoch 1; E1), 11–20 May (Epoch 2; E2), and 21–29 May (Epoch 3; E3). These epochs repeated sampling over a period of time and are representative of sinking particle propagation down to 500 m assuming a particle sinking rate of 50–100 m d^{-1} (i.e., ~ 5–10 d; Siegel et al., 2016). Epochs of approximately these lengths were delineated by two large storms that disrupted sampling. While the storms changed the sampling system, to be discussed extensively, the beginning of the large storms marked the ends of each epoch as sampling was paused. Therefore, E2 and E3 are representative of the system as altered by the most recent large storm.

Vertical mixing in response to storms was apparent in potential

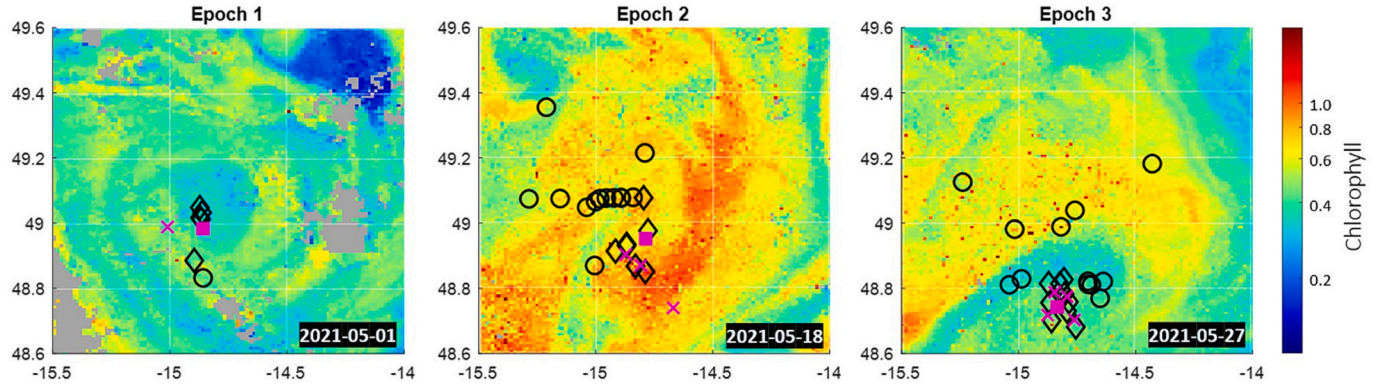

Fig. 1. Composite daily chlorophyll (mg m^{-3}) maps are shown from 3 days representing Epochs 1 (2021-05-01), 2 (2021-05-18), and 3 (2021-05-27). The purple square is the eddy center as determined by autonomous assets on that particular day. Symbols for casts (circles = NEC, diamonds = EC) and pumps (X's, concurrent with thorium casts) are shown, as a function of distance in degrees from the eddy center on the day that they were taken. (For interpretation of the references to colour in this figure legend, the reader is referred to the web version of this article.)

density, saturated oxygen ($O_{2\ sat}$), nitrate (NO_3) and dissolved silica (dSi) data in the eddy center (Johnson et al., 2024). Mixed layer $O_{2\ sat}$ throughout the cruise was >100%, consistent with supersaturation and biological production. With each storm, surface water was mixed with deeper, less oxygenated waters. Nitrate levels in the mixed layer increased after each storm period, but decreased between storms, suggesting that storms generally mixed nutrients upwards where they were then depleted. Mean NO_3 values with standard deviation per epoch were 4.86 ± 0.11 (E1), 4.74 ± 0.38 (E2), and 5.52 ± 0.27 μmol L^{-1} (E3). Mean SiO_4 values with standard deviation per epoch were 0.24 ± 0.11 (E1), 0.52 ± 0.31 (E2), and 1.45 ± 0.21 μmol L^{-1} (E3). Nutrient data cited here are from autonomous gliders and seawater measurement, and detailed further in Johnson et al. (2024), and are consistent with nutrient budget findings in Meyer et al. (2023). Data from deployed gliders show a deepening of the mixed layer on average throughout the cruise, wherein the E1 average was 26 m, E2 was 40 m and E3 was 50 m for casts considered in this study. Furthermore, concentrations of high chlorophyll in the eddy center (1.04 ± 0.14 mg m^{-3}) deepened after E1 and the first storm, but dissipated in intensity throughout E2 (0.93 ± 0.10 mg m^{-3}) to ultimately be <1 mg m^{-3} throughout the water column by E3 (0.66 ± 0.06 mg m^{-3}).

The relatively high nitrate concentrations but low silicate concentrations indicate that the bloom was dominated by siliceous organisms, with nitrate remaining to support an additional bloom of non-silicified phytoplankton (Sieracki et al., 1993; Johnson et al., 2024). Although siliceous organisms other than diatoms exist, three key findings suggest that we were indeed sampling the demise of a diatom-dominated bloom: (1) the low proportion of PIC (< 10%) in the overall carbon pool (this study), (2) HPLC results show diatom-associated fucoxanthin dominated the community at the beginning of the sample period (Meyer et al., 2023), and (3) diatom representation in the organism pool viewed via onboard imaging (H. Sosik, personal comm.). Later in the cruise, however, a modified community of smaller, more diverse phytoplankton emerges. This includes dinoflagellates and haptophytes (Meyer et al., 2023; H. Sosik, personal comm.), with the ratio of small cell to large cell phytoplankton equalizing (Cohn et al., 2023), consistent with previous studies of bloom progression (e.g., Lochte et al., 1993; Henson et al., 2012; Sundby et al., 2016). The demise of a diatom bloom leading into a shift to a smaller, more diverse community structure (Cohn et al., 2023; Meyer et al., 2023) is the biological context driving the evolution of export to be discussed here.

3. Methods

3.1. Sample collection and processing

3.1.1. Total ^{234}Th seawater samples

During the cruise, 800 ^{234}Th seawater samples were collected over 50 CTD casts with high depth resolution (12–17 samples) from the surface to 500 m. Sampling and analysis for total (dissolved + particulate) ^{234}Th was carried out in accordance with the method described in Clevenger et al., 2021. Seawater was collected directly from the shipboard rosette Niskin bottles equipped with a Seabird CTD system. They were then immediately acidified to pH = ~ 1 and spiked with 1 mL ^{230}Th (~ 50 dpm g^{-1}, dpm = disintegrations per minute) to be used as a yield monitor. Following a 6-h equilibration time, sample pH was increased to a pH = 8–9 and reagents were added to form a manganese oxide precipitate, which preferentially scavenges ^{234}Th and ^{230}Th while leaving ^{238}U in solution. Samples were filtered 8 h after precipitation onto 25 mm quartz microfiber filters (QMA), and mounted for beta counting at sea once dry.

Mounted samples were analyzed to ≤3% counting error on one of 6 anticoincidence, 5-position, low-level Risø beta counters with low background activity (average 0.25 counts per minute, cpm). Beta counters were calibrated using low-energy ^{238}U standards, rotated through each of the 30 detectors to obtain detector-by-detector efficiencies. Six of the 30 detectors differed from an average normalized detector efficiency by 4 to 5%, and were adjusted accordingly (Clevenger et al., 2021). For further calibration, 5 deep water (2500 m) samples were rotated through each detector to obtain an overall counter efficiency. Thorium-234 and ^{238}U are assumed to be in secular equilibrium by this depth. The 5 deep water samples, counted on all 30 detectors, had an average activity of 2.44 ± 0.13 dpm L^{-1}.

After samples were allowed to decay for >6 half-lives (at least 144 days), they were recounted to obtain a final sample count rate (cruise average = 0.50 ± 0.06 cpm), which was subtracted from the first count. The final background represents the counter background as well as the activity from non-^{234}Th beta-emitting radionuclides carried by the manganese oxide precipitate. This net cpm value was corrected for ^{234}Th decay and ingrowth, as well as sample volume and method yield to obtain a ^{234}Th activity in dpm L^{-1}. The yield monitor correction was carried out on each sample in accordance with the method detailed in Clevenger et al., 2021, adapted from Pike et al., 2005. The cruise average yield monitor recovery value was 92 ± 8%. Errors reported include first counting error, recovery error, and final counting error. All resulting ^{234}Th activity values are reported in the SeaBASS Data Repository (https://seabass.gsfc.nasa.gov/archive/WHOI/buesseler/EXPORTS/EXPORTSNA/archive/).

3.1.2. Thorium-234, carbon and biogenic silica on size-fractionated particles collected using in situ pumps

In order to obtain element to ^{234}Th ratios (hereafter referred to as element/Th), size-fractionated particles were collected using battery-powered in situ pumps (Large Volume Water Transfer System, McLane Industries) coupled to two 142-mm diameter mini-MULVFS (Multiple Unit Large Volume in-situ Filtration System) filter holders (Bishop et al., 2012; Lam et al., 2015). One filter holder was loaded with three Nitex screens (335, 51 and 5 μm nominal pore size) followed by a pre-combusted QMA filter (~1 μm nominal pore size). Size-fractionated particles from this 4-tier filter system were analyzed for ^{234}Th, particulate carbon (PC), particulate inorganic carbon (PIC), bSi, as well as other analytes (i.e., particulate nitrogen, phosphorus, pigments, ^{210}Po/^{210}Pb, ^{228}Th, Ba isotopic composition, RNA, and other organic compounds). The other filter holder was equipped with a 51 μm Nitex screen followed by a polyethersulfone membrane filter (Supor, 0.8 μm nominal pore size) used for bSi (analyzed only on the Supor filters), and other analytes (i.e., trace metals and organic compounds that will be reported elsewhere). Nitex screens and Supor filters were acid-leached prior to the cruise.

Seven to nine pumps were each deployed for a total of eight casts (1 in E1, 3 in E2, and 4 in E3). In E1 and E2, pumps were deployed at 20, 50, 75, 125, 175, 330 and 500 m, and in E3 at 20, 50, 95, 145, 195, 330, and 500 m (in addition to 35 and 70 m in two casts in E3). The deepest 5 depths in all epochs coincided with the depths of sediment traps deployed in the eddy core by the Process ship (Estapa et al., 2023). A pressure sensor attached to the deepest pump confirmed depths. Pumps were programmed to sample for four to five hours at a starting flow rate of 6 L min^{-1} and pumped on average 1000 L. Approximately 60 samples for each size fraction were collected. Additional filter holders containing a full set of filters, but without any active water pumping, were mounted on the shallowest (20 m) or deepest (500 m) in situ pump to obtain process (or dipped) blanks (n = 7; Lam et al., 2015). On the process blanks, a prefilter (0.2 μm Supor) was placed on top of the 335 μm Nitex screen to avoid the collection of particles while filters were exposed to seawater. After recovering the in situ pumps, the prefilter was discarded and the process blanks were processed in the same manner as the samples. Immediately after recovering the pumps, residual water from each filter holder was removed by vacuum to avoid particle loss.

Filter processing was conducted in a clean-air bench placed in a HEPA-filtered work space following the protocols used during the EXPORTS North Pacific cruise (Buesseler et al., 2020b; Roca-Martí et al., 2021). Zooplankton that were not part of the passive sinking flux ("swimmers") and were visible to the naked eye were handpicked from the 335 μm screens using forceps. Particles were gently rinsed off the Nitex screens onto 25 mm diameter 1.2 μm pore-size silver (Ag) filters using 0.1 μm prefiltered refrigerated seawater from 500 m depth. At five stations the entire screens were rinsed, whereas at three stations the screens were cut in half using a stainless-steel rotary blade (45 mm) to allow for further analyses of geochemical constituents (Cutter et al., 2017). QMA filters were subsampled for ^{234}Th, PC, and PIC using circular punches of 22–25 mm diameter. QMA and Ag filters were dried in a 50–60 °C oven, beta counted at sea for ^{234}Th activities and recounted six months later on shore for background activities. After counting, screen samples that had been rinsed onto Ag filters were split by weight (Lamborg et al., 2008), and ~ 1/3 of each sample was analyzed for PC, PIC and bSi. Biogenic silica was also measured on a subsection (1/8) of the Supor filters (kept frozen after collection until processing). Particulate carbon was analyzed using high-temperature combustion on a Costech 4010 Elemental Analyzer. Particulate inorganic carbon was determined by coulometric titration using a CO_2 coulometer (model CM5014, UIC Inc.). Each sample was placed in a glass vial secured to a CM5130 acidification module and treated with 2 mL of 1 N H_3PO_4 to liberate the CO_2 into a closed system to be measured (Honjo et al., 1995). Biogenic silica was determined by following the 0.2 M NaOH digestion method (40 min at 95 °C followed by neutralization with 1 M HCl; Brzezinski and Nelson, 1989) and spectrophotometric detection (UV–Visible Spectrophotometer, Genesys 10S, Thermo Scientific).

The average of all process blanks was subtracted from total ^{234}Th, PC, PIC, and bSi measurements. Process blanks were < 3% of the total ^{234}Th, PC and bSi measured on the filters (Ag filters: 0.07 ± 0.10 dpm ^{234}Th; 1/3 Ag filters: 0.58 ± 0.49 μmol C, 0.04 ± 0.06 μmol Si; QMA punches: 0.06 ± 0.09 dpm ^{234}Th, 0.56 ± 0.45 μmol C; 1/8 Supor filters: 0.02 ± 0.02 μmol Si). Particulate inorganic carbon process blanks accounted for 15% of the measured PIC on 1/3 Ag filter (i.e. screen rinses; 0.70 ± 0.37 μmol C) and 28% of PIC on the QMA punches (0.25 ± 0.03 μmol C). Triplicate QMA punches from three samples (20, 175, 500 m) were analyzed for PC and PIC, obtaining a relative standard deviation of 4–6% and 4%, respectively. These values indicate that particle distribution was relatively even across the QMA filters and support the reproducibility of the subsampling method (Maiti et al., 2012). Particulate organic carbon concentrations were obtained from the difference between blank-corrected PC and PIC results (PIC averaged ≤10% of PC in all size fractions). Biogenic silica for the 1–5 μm size fraction was obtained from the difference between blank-corrected bSi from the 0.8–51 μm (Supor filters) and the 5–51 μm (5 μm Nitex screens) size fractions. Data for POC and bSi have associated uncertainties derived from the blank corrections, and particulate ^{234}Th from the blank corrections and counting. Size-fractionated particle data from the 2021 EXPORTS expedition are found in the SeaBASS Data Repository https://seabass.gsfc.nasa.gov/archive/WHOI/buesseler/EXPORTS/EXPORTSNA/archive/).

3.2. Thorium-234 data analysis

3.2.1. Thorium-234 activity and steady state flux analysis

Generally, ^{234}Th flux can be calculated using a ^{234}Th activity balance described by the following equation:

$$\frac{d\,^{234}Th}{dt} = {}^{238}U\lambda_{^{234}Th} - {}^{234}Th\lambda_{^{234}Th} - E + V \quad (1)$$

where ^{234}Th (dpm L^{-1}) is the total ^{234}Th activity, ^{238}U (dpm L^{-1}) is the ^{238}U activity, $\lambda_{^{234}Th}$ (0.0288 d^{-1}) is the decay constant of ^{234}Th, E (dpm L^{-1} d^{-1}) is the net export of ^{234}Th from adsorption onto sinking particles, and V (dpm L^{-1} d^{-1}) is the sum of advective and diffusive fluxes of ^{234}Th. If we assume a steady state (SS) case where $d\,^{234}Th/dt = 0$ and assume that advective and diffusive fluxes are negligible compared to production and decay rates (V = 0), the downward flux of ^{234}Th on particles can then be determined by integrating the deficit of ^{234}Th relative to ^{238}U over a given depth (z), in accordance with the following equation:

$$E = \int_0^z \left(\lambda_{^{234}Th}\left({}^{238}U - {}^{234}Th\right)\right)dz \quad (2)$$

3.2.2. Thorium-234 non-steady state analysis

In some situations, when repeat sampling allows for time-series measurements of the same water mass, a non-steady state (NSS) case must be considered where $d\,^{234}Th/dt \neq 0$ (Savoye et al., 2006). Note that in these cases, advective and diffusive fluxes are still most often considered negligible. A NSS model is needed when there are increases or decreases in export that cause a change in ^{234}Th activities versus time within the time frame of ^{234}Th's half-life (24.1 d). The SS assumption can underestimate ^{234}Th removal when there is intense scavenging, or can overestimate ^{234}Th removal during post-bloom conditions (Buesseler et al., 1992; Ceballos-Romero et al., 2018). Based on both the sampling scheme of the 2021 EXPORTS cruise discussed in Section 2, and the rapidly changing bloom conditions during the sampling period, the data presented here is an ideal candidate for NSS analysis.

A number of factors specific to this study's data and previous literature support the use of a NSS model over a SS model. The North Atlantic

bloom represents a dynamic biological ecosystem with changes on a timescale less than the ^{234}Th half-life (Brown et al., 1985; Esaias et al., 1986; Buesseler et al., 1992; Savoye et al., 2006; Ceballos-Romero et al., 2018), suggesting that an NSS model should be used. Previous studies of this PAP site during a bloom (e.g. Buesseler et al., 1992; Le Moigne et al., 2013) show that, generally, ^{234}Th flux values are >800 dpm m^{-2} d^{-1}, which is the flux threshold over which Savoye et al., 2006 suggests reoccupation of a sample site for NSS analysis. Indeed, analysis of the data in this experiment revealed ^{234}Th flux values that are significantly lower than previous studies when calculated using the simple SS model. Further, ^{234}Th activities when considered in distinct depth bins clearly decrease with time (example shown in Fig. 2) indicating that the NSS analysis of this data is more appropriate than SS analysis.

It was decided to break casts into two groups for a Lagrangian time-series analysis: eddy center (EC; < 15 km from eddy center; $n = 23$), and non-eddy center (NEC; > 15 km from eddy center; $n = 27$), although a number of iterations of groupings were considered (see Supplemental Information). Once groups were chosen, ^{234}Th activities from each cast were averaged within 9 depth bins to 500 m – the same bins for each of the two groups – and $d\,^{234}Th/dt$ values were calculated using a linear fit of ^{234}Th activity values over time from the first cast. Fits and corresponding errors (uncertainty within one standard deviation) across the 9 depth bins for both groups can be found in Table 1. An example of the ^{234}Th activity versus time plot used to calculate $d\,^{234}Th/dt$ values is shown in Fig. 2, using a set of data (20–50 m depth bin in the EC grouping) that is representative of the trend found in all depth bins for each of the two groups, particularly in the upper water column where the relationship is the strongest. Beyond the derivation of discrete $d\,^{234}Th/dt$ values in the 9 depth bins chosen, linear fits between the $d\,^{234}Th/dt$ values at the midpoint depth of each of the 9 depth bins were produced, and the resulting linear equations were used to define a specific $d\,^{234}Th/dt$ for each sample at any given depth. In other words, the specific depth of each sample had its own $d\,^{234}Th/dt$ value derived from linear fits between the overall bin $d\,^{234}Th/dt$ values (see Supplemental Fig. 1 for depth profiles of NSS terms and resulting linear fits).

In this study, we derived NSS flux according to the following modification of Eq. 1:

$$Flux_{NSS} = \left[\left(^{238}U - {}^{234}Th\right)\lambda_{^{234}Th} - \left(\frac{d^{234}Th_{Specific}}{dt}\right) * 1000 \right] * depth\ integral \tag{3}$$

where the depth integral is in (m) units, and the $d\,^{234}Th/dt$ term is the sample-specific term described above. The above equation allows for derivation of NSS fluxes for distinct depth bins, and then derivation of NSS fluxes throughout the entire water column. This results in high resolution, sample-by-sample derivation of NSS fluxes.

3.3. Physical transport effects on ^{234}Th fluxes to validate ^{234}Th analysis

The SS equation described in Section 3.2.1 (Eq. 2) is a 1-D accounting that ignores the impacts of physical transport and temporal variability in ^{234}Th activities by assuming these terms are relatively small. However, to assess the uncertainties tied to this assumption, we examined ^{234}Th export inside a simulated tracked eddy using an idealized double gyre, submesoscale permitting physical model coupled with a simplified biogeochemical model with explicit ^{234}Th cycling (Resplandy et al., 2012; Resplandy et al., 2019). In-brief, the physical model was run at a 1/54 degree (2 km) horizontal resolution and forced using climatological atmospheric forcing. A lower resolution output (1/9°) from this physical model was used to run the offline biogeochemical model (LOBSTER) to calculate the biogeochemical cycling (temporal component) of nitrate, ammonium, one phytoplankton, one zooplankton, and two size-classes of detritus. This lower resolution of the physical model was previously shown to have an almost indistinguishable impact on the

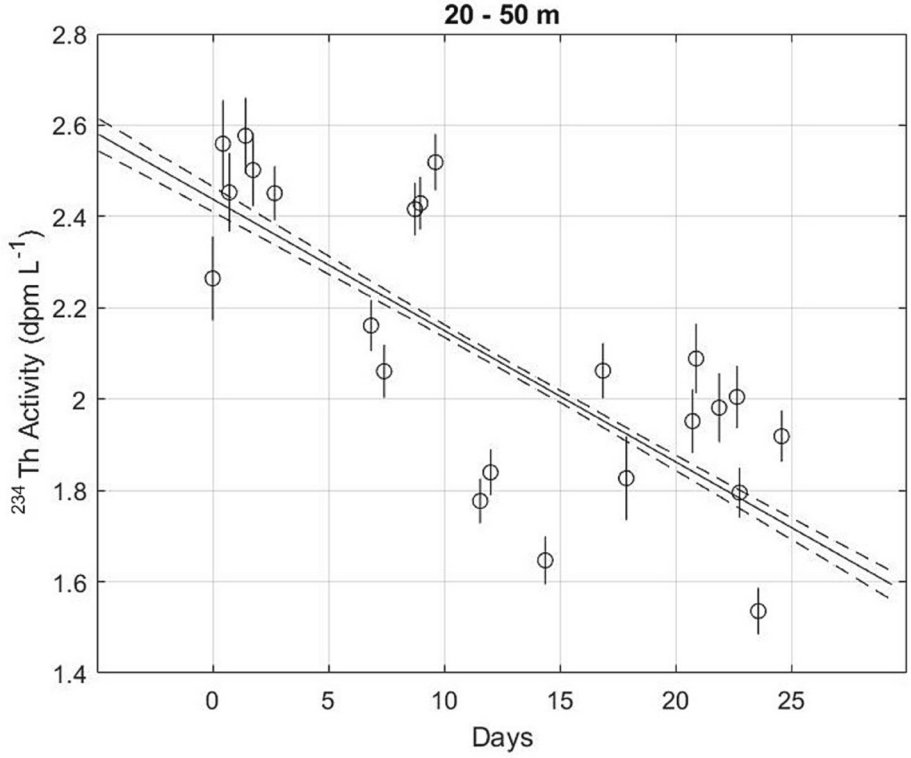

Fig. 2. An example of the ^{234}Th activity versus day from the first sample, used to derive dTh/dt for non-steady state calculations. This specific set of data is the 20–50 m depth bin for the eddy center (EC) grouping. The linear decrease in activity versus time in a particular depth bin is indicative of a system that is not in steady state.

Table 1
Non-steady state (NSS) terms at 9 depths bins for the EC and NEC groups, derived from linear fits of ^{234}Th activity (dpm L^{-1}) over time (d) for the entire duration of the sampling period. Depth profiles of NSS terms can be seen in Supplemental Fig. 1.

EC									
Depth Bins (m)	0–20	20–50	50–75	75–95	95–125	125–150	150–200	200–300	300–500
dTh/dt (dpm L^{-1} d^{-1})	−0.0254	−0.0287	−0.0278	−0.0231	−0.0223	−0.0077	−0.0063	−0.0064	−0.0045
Error	8%	6%	7%	10%	8%	28%	30%	33%	45%
R^2	0.54	0.58	0.49	0.42	0.39	0.34	0.23	0.13	0.1

NEC									
Depth Bins	0–20	20–50	50–75	75–95	95–125	125–150	150–200	200–300	300–500
dTh/dt (dpm L^{-1} d^{-1})	−0.0217	−0.0224	−0.0239	−0.0352	−0.0368	−0.0142	−0.0109	−0.0029	−0.0013
Error	12%	9%	9%	8%	6%	19%	22%	87%	194%
R^2	0.41	0.45	0.38	0.50	0.50	0.22	0.32	0.07	0.01

biological tracers. Explicit ^{234}Th cycling is included per Resplandy et al. [2012], which results from the processes of radioactive decay, particle adsorption/desorption, ecosystem cycling, detritus aggregation/disaggregation, and remineralization. The model solution is not specific to the cruise period (forcing is climatological) but it captures the North Atlantic bloom dynamics and reproduce the range of ^{234}Th-based export in the region (see further details and evaluation in Resplandy et al., 2012 and Resplandy et al., 2019).

From the model output, a mesoscale, anticyclonic simulated-eddy (sim-eddy) similar to the cruise eddy and located in the subpolar gyre was identified and tracked within the model using closed contours of sea surface height (SSH) anomalies. The sim-eddy was roughly ½ degree (50 km) in diameter and thus comparable in size with the cruise eddy (core diameter 30 km; Johnson et al., 2024). In addition, modeled sub-surface (~75 m depth) horizontal ^{234}Th gradients in the vicinity of the sim-eddy reached ~0.3 dpm km^{-1}, similar to the observed cruise eddy gradients (~0.2 dpm km^{-1}), calculated between 75 m-depth cruise samples separated by a minimum of 1 km and a maximum of 15 km, and taken within two days of each other (similar to the model output frequency). The sim-eddy core was defined as a 2 × 2-degree box at the center of the SSH contour, which captures a radius of 12.5 km from the eddy center (similar to the 15 km radius used to define EC samples in the cruise eddy). The 30-day period of the sim-eddy lifespan that most closely paralleled cruise observations was chosen to quantify the contribution of physical transport to the ^{234}Th export flux and evaluate the potential uncertainty associated with the assumption that physical transport is small in the eddy center.

From model output specific to the eddy center, we determined the percentage of the total simulated ^{234}Th downward flux that was due to physical transport and compared it to the percentage of the NSS term determined from Eq. 3 above (Table 2). The total modeled physical transport was 11% of the total NSS ^{234}Th flux at 75 m, increasing to 27% of the total NSS ^{234}Th flux at 550 m. These percentages are generally within the error of the total flux measurements presented in this study, supporting the assumption that the physical transport term is small in the center of a coherent eddy.

Table 2
Comparison of data from a simulated eddy model, to actual data from this study (EC group, average over all epochs).

	Model Data			Study Data		
Depth	Total Flux	Phys Trans % of Total	dTh/dt % of Total	Depth	Total Flux	dTh/dt % of Total
75	2721	11	43	75	2903	78
91	3133	11	44	90	3309	81
135	3739	14	39	125	3720	88
170	4044	15	36	175	3721	97
335	5013	21	37	330	3786	80
550	5398	27	43	500	3795	73

The real-world cruise system was influenced by a number of storms (storm days making up 42% of cruise period), causing entrainment velocity ($w_E = \frac{\partial H}{\partial t}$ where H is MLD) to range from 10 to 35 m d^{-1}, and surface core waters (defined by the depth of the 27.1 isopycnal) to account for 40% of the T and S variability observed by autonomous assets within the eddy center (Johnson et al., 2024). Analysis of tracer flux suggests that advection played a larger role in particulate movement dynamics than entrainment did, whereas entrainment played a larger role in nutrient concentrations (Johnson et al., 2024; Meyer et al., 2023). Although the physical effects of advection and entrainment certainly contribute to uncertainty and variability of the results of this study, particularly in the surface waters, this sim-eddy comparison is useful to obtain a baseline assessment of the impact of physical transport in an ideal system within the EC waters.

The physical transport terms around the edges, outside of the 15 km radius EC boundary, are expected to be somewhat larger (Resplandy et al., 2012). Given that derivation of these terms specific to the cruise-eddy is outside of the scope of this paper, discussion will focus largely on data from the EC to minimize the uncertainties associated with physical transport on our estimates. Presentation and interpretation of NEC data is a focus of future work.

3.4. Analysis of biological carbon pump characteristics

Upper-ocean BCP efficiency was assessed by the ratio between POC export out of the Ez relative to integrated NPP in the Ez (Ez-ratio = $Flux_{Ez}$/NPP) and the transfer efficiency of POC through the upper twilight zone ($T_{100} = Flux_{Ez+100m}/Flux_{Ez}$) (Buesseler and Boyd, 2009). The extent to which POC that is produced is then exported out of the sunlit zone, and then how much reaches deeper in the water column, is controlled at least by the following factors: the amount of primary production (De La Rocha and Passow, 2007), particle sinking velocity (De La Rocha and Passow, 2007), the rate of remineralization (Le Moigne et al., 2016), mineral ballasting of particles that influences particle sinking rates (De La Rocha and Passow, 2007; Le Moigne et al., 2014), injection of POC to depth by vertical migration among other processes (Boyd et al., 2019), and zooplankton feeding (Cavan et al., 2015; Le Moigne et al., 2015).

We defined a unique Ez base depth for each cast, rather than a fixed depth, allowing for a cast-specific assessment and a more informative comparison of BCP efficiencies (Buesseler et al., 2020a). This is because the Ez base depth often differs between sampling sites. Even small differences in Ez depths can affect comparisons of BCP efficiencies relative to organic matter production and gradients in POC flux just below the Ez (Buesseler et al., 2020a). Here, in order to compare data to previous work and conduct a cast-specific analysis, we calculated the BCP characterizing-metrics, the Ez-ratio and T_{100}, using both a fixed 100 m Ez depth and cast-specific Ez depth definitions based on in situ

fluorescence data. For depth-integrated NPP estimates, the depth of the base of the Ez was defined as 0.1% of the maximum photosynthetically available radiation ($PAR_{0.1}$) (J. Fox, personal communication). Depth-integrated NPP values were calculated using discrete carbon uptake measurements from ^{14}C analysis of multi-day incubations, and are as follows: 90 ± 10 (E1), 82 ± 13 (E2), and 54 ± 9 mmolC m^{-2} d^{-1} (E3). Depth profiles of NPP were integrated using trapezoidal integration to 0.1% light levels using Compact-Optimal Profiling System (C-OPS) estimates of PAR % depths. However, ^{234}Th sample collection was often done during the night with significant cloud cover. Sample timing combined with sensor malfunctions resulted in only 46% of sampled casts having a known $PAR_{0.1}$ value. Therefore, as a proxy for systematically defining the Ez for each cast we used the primary production zone (PPZ), defined as the depth at which the signal from in situ fluorescence sensors dropped to 10% of the maximum above that depth (Owens et al., 2015). The 10% definition was chosen by Owens et al. (2015) as a conservative estimate that delineates between surface water where chlorophyll pigment is present, and deeper water where not enough light is present to maintain chlorophyll. Table 3 shows NPP and depth horizon (MLD, PPZ, PAR1%, PAR0.1%) values with standard deviations of the all-cast (NEC and EC group inclusive) means. We considered the PPZ depth to be a boundary below which there is no further production of fresh POC due to photosynthesis. The use of PPZ allows for comparisons of BCP efficiencies between sites that have different particle sources, remineralization efficiencies, and weather patterns. The PPZ is found to be several meters to tens of meters below $PAR_{1.0}$, but is typically closer to $PAR_{0.1}$ (Marra et al., 2014; Owens et al., 2015). As chlorophyll pigments that are used to define PPZ have a lifetime of multiple days (e.g., Lacour et al., 2019), PPZ measurements should be seen as a multiday average boundary for organic matter production (Buesseler et al., 2020a).

4. Results

4.1. Thorium-234 flux results

Thorium-234 activity with depth by epoch is shown in the top row of Fig. 3 (EC) and Supplemental Fig. 2 (NEC). Average ^{234}Th activities below the epoch-specific PPZ were consistently larger than ^{238}U activities in all epochs regardless of location. In a typical SS system, ^{234}Th activity profiles would show a deficit relative to ^{238}U at depth in the Ez indicative of export ($^{234}Th < {}^{238}U$), excess of ^{234}Th ($^{234}Th > {}^{238}U$) near the base of the Ez, and equilibrium ($^{234}Th = {}^{238}U$) in deeper waters. An excess of ^{234}Th compared to ^{238}U is indicative of a source of ^{234}Th, such as respiration or remineralization of sinking particles. The overall temporal trends of average ^{234}Th activities with depth show that zones of export and remineralization change by epoch with the deepening of the PPZ. In each epoch average activity profile (first row, Fig. 3 and Supplemental Fig. 2), export (activity deficit) can be seen until reaching equilibrium and remineralization (activity excess) starts at approximately the epoch average PPZ depth. It is noteworthy that this excess persists through 500 m, the base of the measurement zone, rather than reaching equilibrium in a canonical manner. This is indicative of a system that is out of steady state.

Table 3
Net primary productivity epoch averages. Epoch average depth horizons (mixed layer depth, primary production zone, 1% photosynthetically available radiation, 0.1% photosynthetically available radiation), averaged over all casts. Standard deviations of all measurements included. NPP (mmol m^{-2} d^{-1})is integrated to PAR0.1%.

	NPP	MLD	PPZ	PAR1%	PAR0.1%
E1	90 ± 10	26 ± 6	65 ± 7	37 ± 1	56 ±2
E2	82 ± 13	40 ± 17	93 ± 18	51 ± 12	76 ± 17
E3	54 ± 9	50 ± 29	127 ± 22	51 ± 4	76 ± 7

If we applied a SS ^{234}Th model for all data, regardless of location, epoch average ^{234}Th flux would range between approximately −3200 ± 700 to 1700 ± 200 dpm m^{-2} d^{-1} (second row, Fig. 3 and Supplemental Fig. 2; Supplemental Table 1). To find such an excess of ^{234}Th throughout the subsurface would mean there is some constant source of ^{234}Th that is unsustainable given the lack of an equal deficit above. The SS component in this case describes an imbalance between surface export and mesopelagic accumulation of ^{234}Th. Using an NSS model accounts for variations over the course of the survey, where mesopelagic accumulation is low from E1 to E3, and the excess of ^{234}Th observed at E1 gradually decreases towards secular equilibrium. It could be hypothesized that the SS results observed in E1 are inherited from export and accumulation of ^{234}Th that may have occurred before our cruise period. We provide average SS flux values per epoch in Supplemental Table 1, however, this is for comparative reasons only and should not be viewed as a lower limit on fluxes during EXPORTS.

When the NSS model is applied, ^{234}Th fluxes increase between epochs, and generally increase from cast to cast within each epoch (second row, Fig. 3 (EC) and Supplemental Fig. 2 (NEC)). Cast-to-cast increase for EC casts can be seen in Supplemental Fig. 3, which shows that variability in the dataset within epochs is typically temporal in nature. Epoch-average, maximum ^{234}Th fluxes with standard deviation are as follows: 2900 ± 890 (E1; 125 m), 4100 ± 1760 (E2; 410 m), and 5400 ± 1680 dpm m^{-2} d^{-1} (E3; 500 m) for EC; and 3000 ± NA (E1; 150 m), 5400 ± 440 (E2; 225 m), and 6000 ± 800 dpm m^{-2} d^{-1} (E3; 225 m) for the NEC. Average fluxes with standard deviation at 500 m are: 2200 ± 1400 (E1), 3800 ± 2000 (E2), and 5400 ± 1680 dpm m^{-2} d^{-1} (E3) for EC; and 2000 ± NA (E1), 4500 ± 1680 (E2), and 5400 ± 900 dpm m^{-2} d^{-1} (E3) for NEC. Average fluxes and standard deviations at the all-epoch average PPZ depths (closest depth sampled) are as follows: 2300 ± 270 (E1; PPZ = 67 m), 3300 ± 700 (E2; PPZ = 90 m), 4600 ± 680 dpm m^{-2} d^{-1} (E3; PPZ = 133 m) for EC; 1300 ± NA (E1; PPZ = 53 m), 3800 ± 500 (E2; PPZ = 94 m), and 5400 ± 530 dpm m^{-2} d^{-1} (E3; PPZ = 122 m) for NEC). Average EC NSS flux values per epoch can be found in Table 4, average NEC NSS flux values per epoch can be found in Supplemental Data Table 2, and all NSS flux data per cast can be found in Supplemental Data Table 3.

4.2. Particulate organic carbon and biogenic silica ratios

The use of POC/Th and bSi/Th ratios in pump samples to determine element fluxes from ^{234}Th fluxes assumes that the particles in the pump samples represent the majority of sinking particles at the depth and time of ^{234}Th flux measurement. This assumption fails only if a significant fraction of the sinking flux is carried by particles that differ in POC/Th and bSi/Th, which we assess by comparing results from pumps and sediment traps deployed at the same depths and times during EXPORTS (75–500 m, Fig. 3; shallow pumps were excluded from this analysis). The sediment trap data can be found in the SeaBASS Data Repository (https://seabass.gsfc.nasa.gov/archive/Maine/Estapa/EXPORTS/EXPORTSNA/). The >5 μm pump size fraction (i.e., combination of 5–51, 51–335, and > 335 μm size fractions) rather than the >1–5 μm size fraction or a single size fraction (Fig. 4) was used to derive POC and bSi fluxes for the following reasons: (1) bSi/Th ratios in the smallest size fraction (1–5 μm) were an order of magnitude lower than in traps (0.14 ± 0.10 vs. 0.9 ± 0.2 μmol dpm^{-1}, respectively), whereas 5–51, 51–335, and > 335 μm (1.1 ± 0.2, 1.3 ± 0.6, 1.3 ± 0.2 μmol dpm^{-1}, respectively) were similar to traps (Fig. 4); (2) POC/Th ratios in the >5 μm size fraction better matched traps relative to the >1 μm size fraction in epochs 1 and 2, and the >5 μm fraction captured the decreasing temporal trend observed in traps; and (3) while the POC/Th and bSi/Th in the >5 and > 51 μm size fractions were very similar (Fig. 3), we chose the >5 μm as it represented a larger fraction of the particulate material.

The pump casts showed temporal variability in POC/Th and bSi/Th ratios across epochs (Fig. 5). In studies with less temporal variability in the system over the sampling period (e.g., Buesseler et al., 2020b), it has

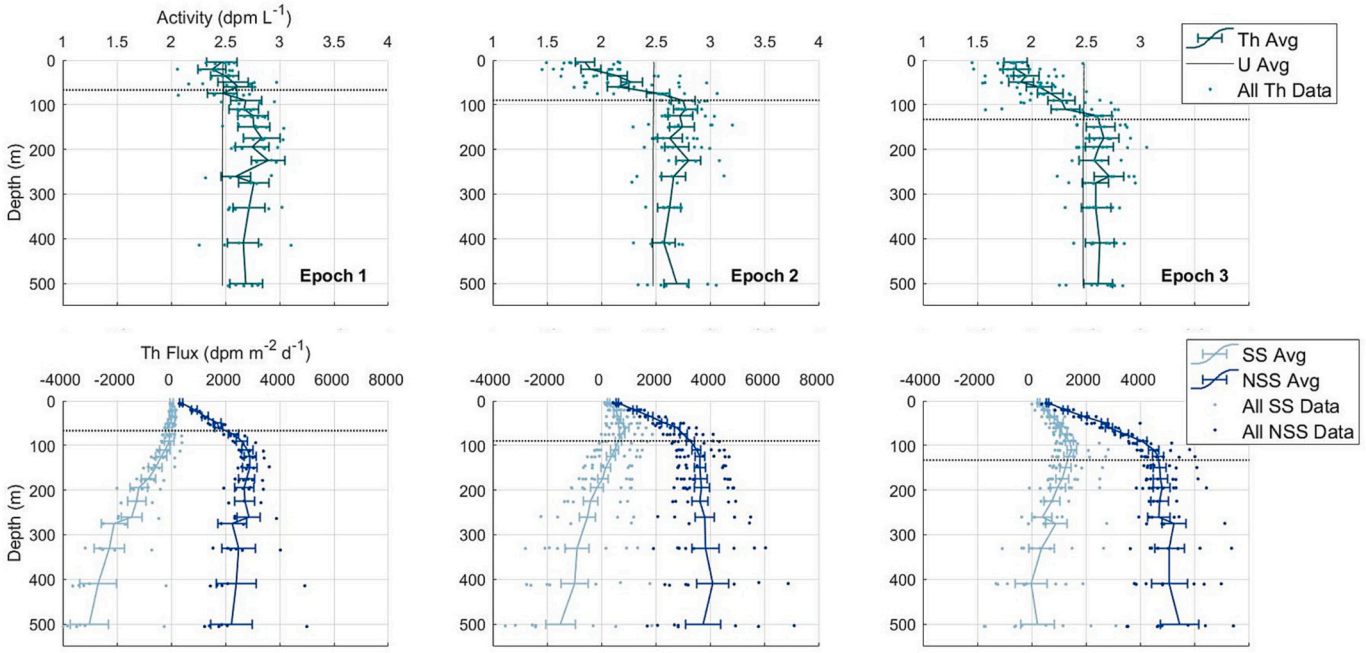

Fig. 3. The 6 panels in this figure show: (Top row) thorium-234 and uranium-238 activity with depth, error bars represent counting and processing error, and (bottom row) thorium-234 flux from both steady state (SS) and non-steady state (NSS) models, error bars represent cumulative error from thorium measurements and error from the NSS analysis. Data is from casts in the eddy center (EC). In all subplots, individual data points show all measurements taken in that epoch, while the line and error bars represent the epoch average. Horizontal dotted lines show the average PPZ of all EC casts for that particular epoch.

been possible to use an overall average of all pump casts to obtain depth-specific POC/Th ratios. Due to the temporal variability in this system, however, epoch-specific POC/Th and bSi/Th ratios from pump casts were applied to NSS ^{234}Th flux values to estimate POC fluxes.

Fits and corresponding errors were derived in two parts through the depth profiles: (1) at shallower pump depths, ratios decrease linearly (except for bSi/Th in E3), therefore a slope is found with a simple linear fit and a percent error is calculated from the average individual uncertainties of the measurements, and (2) at deeper pump depths, data were averaged across depths, where error is applied as the standard deviation between those data points. Differences in these can be seen in Fig. 5. This is consistent with how element/Th ratio analysis has been carried out in previous ^{234}Th studies (Black et al., 2018; Buesseler et al., 2020b; Kenyon, 2021). Only one set of epoch-by-epoch POC/Th and bSi/Th values were applied to ^{234}Th flux profiles from the corresponding epoch, regardless of location in relation to the eddy center. It should be noted that ratios from above the MLD are extrapolated from fewer pumps in a regime with complex mixing dynamics, and thus the strongest application of this method is below the PPZ.

Epoch-by-epoch temporal variation in POC/Th ratios (> 5 μm size fraction) derived from McLane pump sampling is most apparent in the shallower pump depth linear fits (Fig. 5). The sharp ratio attenuation in the upper water column goes from the surface to ~50 m in E1, ~ 75 m in E2, and ~ 95 m in E3, before becoming constant beneath those depths to the deepest sampled depth at 500 m. Further, there are differences in the rate of decrease in POC/Th versus depth in the upper water column in the three epochs. The fastest decrease versus depth is observed in E2 (slope = −6.63), then E1 (−8.60), then E3 (−9.28 m dpm μmolC^{-1}). This is consistent with the deepening of the MLD and remineralization layer throughout the cruise and supports the decision not to apply a single cruise-average POC/Th fit. Based on the derived linear fits, the POC/Th ratios with error that were applied to ^{234}Th flux values fall in the following ranges: 10 ± 2 to 4.0 ± 0.3 μmol dpm^{-1} (E1), 14 ± 3 to 3.2 ± 0.3 μmol dpm^{-1} (E2), and 12 ± 2 to 3.1 ± 0.5 μmol dpm^{-1} (E3). Note that in E3, the position of the pump targeting the base of the Ez changed from 75 m (the depth in E1 and E2) to 95 m to capture the observed deepening of the PPZ and MLD.

In the same manner as POC/Th ratios, bSi/Th ratios were derived from pump data. These bSi/Th ratios (> 5 μm size fraction) can be seen in Fig. 5, and are notable in that the slope of bSi/Th linear attenuation in the surface waters becomes less steep from E1 to E2, and bSi/Th ratios remain constant throughout the upper 500 m by E3. Surface bSi/Th ratios decrease by >50% between E1 and E3, while mesopelagic ratios increase by nearly 50% in that same time. Based on derived linear fits, the bSi/Th ratios that were applied to ^{234}Th flux values fall in the following ranges: 2.6 ± 0.5 to 0.9 ± 0.1 μmol dpm^{-1} (E1), 2.1 ± 0.5 to 1.0 ± 0.1 μmol dpm^{-1} (E2), and consistently 1.3 ± 0.1 μmol dpm^{-1} (E3).

Sediment trap-derived ratios are included for comparison purposes (Fig. 5, magenta diamonds). The ^{234}Th flux tracer method relies on the assumption that pump-derived data is representative of overall sinking particles, and sediment traps are an alternative means of analyzing sinking particles. A *t*-test confirms that at a 5% significance level, the POC/Th ratio data is statistically the same in two out of three epochs (E1 and E3), and the bSi/Th ratio data is statistically the same in one out of three epochs (E2). More importantly for the application of this data, the largest deviation between corresponding pump and trap values was 39% of the average value of the two, with the average deviation of all 6 being 23%. The differences in pump and sediment trap data could be due to the breakup of marine snow going through pumps, causing the loss of carbon and thorium associated with smaller particles, thereby increasing the bSi/Th ratio compared to trap data. This would affect carbon and thorium, so would not be apparent in the POC/Th ratios from pumps. If we consider sediment trap data as alternative bSi/Th ratios, bSi fluxes derived from pumps could be overestimated by an all-epoch average of 27% with a standard deviation of 17%. However, with large errors these results are not unexpected nor are they necessarily indicative of a failed sinking particle composition assumption.

4.3. Particulate organic carbon flux results

Epoch-average particulate organic carbon fluxes with a standard

Table 4
Epoch average measurements (non-steady state ^{234}Th fluxes, POC, and bSi fluxes) for the eddy center (EC) group, and associated errors.

Epoch Averages										
EC										
	Depth	NSS Flux	Error	SD	POC Flux	Error	SD	bSi Flux	Error	SD
	(m)	dpm m-2 d-1	dpm m-2 d-1	dpm m-2 d-1	mmol m-2 d-1	mmol m-2 d-1	mmol m-2 d-1	mmol m-2 d-1	mmol m-2 d-1	mmol m-2 d-1
	5	369	69	59	3.6	0.9	0.5	0.9	0.3	0.1
	20	853	107	125	6.7	1.4	1.0	2.0	0.5	0.3
	35	1243	123	99	7.8	1.5	0.6	2.7	0.6	0.2
	50	1698	151	261	7.0	0.9	1.1	3.2	0.7	0.5
	60	1747	146	104	7.0	0.8	0.5	3.2	0.7	0.2
	75	2292	183	266	9.1	1.0	1.1	3.6	0.8	0.4
	90	2607	198	330	10.4	1.2	1.3	3.4	0.8	0.4
	110	2810	216	333	11.2	1.2	1.3	3.0	0.7	0.3
	125	2911	232	326	11.6	1.3	1.3	2.6	0.3	0.3
	150	2884	263	408	11.5	1.4	1.6	2.6	0.3	0.4
	175	2787	295	366	11.1	1.5	1.5	2.5	0.3	0.3
	195	2689	363	499	10.7	1.7	2.0	2.4	0.4	0.4
	225	2709	360	595	10.8	1.7	2.4	2.4	0.4	0.5
	260	2855	436	887	11.4	2.0	3.5	2.5	0.4	0.8
	275	2256	529	580	9.0	2.2	2.3	2.0	0.5	0.5
	330	2478	624	841	9.9	2.6	3.4	2.2	0.6	0.7
	410	2402	731	1429	9.6	3.1	5.7	2.1	0.7	1.3
Epoch 1	500	2220	773	1394	8.9	3.2	5.6	2.0	0.7	1.2
	5	583	48	101	8.1	1.7	1.4	1.2	0.3	0.2
	20	1219	72	222	14.2	2.8	2.6	2.2	0.6	0.4
	35	1800	90	336	17.0	3.3	3.1	2.9	0.7	0.5
	50	2307	106	484	16.3	3.2	3.6	3.2	0.8	0.7
	60	2777	109	590	15.7	3.1	3.0	3.5	0.9	0.7
	75	3003	130	680	9.8	1.2	2.3	3.2	0.4	0.7
	90	3265	150	709	10.4	1.0	2.3	3.4	0.3	0.7
	110	3486	163	716	11.2	1.1	2.3	3.7	0.3	0.7
	125	3619	179	758	11.6	1.1	2.4	3.8	0.3	0.8
	150	3610	207	767	11.6	1.2	2.5	3.8	0.4	0.8
	175	3655	229	829	11.7	1.2	2.7	3.8	0.4	0.9
	195	3683	277	922	11.8	1.3	3.0	3.9	0.4	1.0
	225	3619	301	1099	11.6	1.4	3.5	3.8	0.4	1.2
	260	3778	354	1658	12.1	1.6	5.3	4.0	0.5	1.7
	330	3818	510	1491	12.2	2.0	4.8	4.0	0.6	1.6
	410	4087	582	1761	13.1	2.2	5.6	4.3	0.7	1.8
Epoch 2	500	3726	643	1949	11.9	2.3	6.2	3.9	0.7	2.0
	5	580	54	104	7.1	1.3	1.3	0.8	0.1	0.1
	20	1243	83	191	13.4	2.2	2.1	1.6	0.2	0.3
	35	1924	104	245	17.6	2.8	2.3	2.5	0.2	0.3
	50	2670	122	647	19.9	3.1	4.5	3.5	0.3	0.8
	60	2832	130	243	18.5	2.9	1.7	3.7	0.3	0.4
	75	3413	147	255	16.7	2.6	1.1	4.5	0.3	0.3
	90	4053	172	497	12.7	2.1	1.3	5.4	0.4	0.7
	110	4488	187	673	13.8	2.4	2.1	5.9	0.4	0.9
	125	4629	203	674	14.2	2.5	2.1	6.1	0.5	0.9
	150	4702	234	647	14.4	2.6	2.0	6.2	0.5	0.9
	175	4722	259	670	14.5	2.6	2.1	6.2	0.5	0.9
	195	4785	306	783	14.7	2.7	2.4	6.3	0.6	1.0
	225	4690	323	388	14.4	2.7	1.2	6.2	0.6	0.5
	260	4662	408	633	14.3	2.8	1.9	6.2	0.7	0.8
	275	5238	441	1270	16.1	3.1	3.9	6.9	0.7	1.7
	330	5061	536	1115	15.5	3.2	3.4	6.7	0.8	1.5
	410	5054	663	1126	15.5	3.4	3.5	6.7	1.0	1.5
Epoch 3	500	5439	696	1676	16.7	3.6	5.1	7.2	1.0	2.2

deviation range calculated using the NSS are shown in Fig. 6 (EC) and the third row of Supplemental Fig. 2 (NEC), and epoch average POC flux data can be found in Table 4 (EC) and Supplemental Table 2 (NEC). Within the EC group, epoch averaged maximum POC fluxes with standard deviation increased by epoch from approximately 11.6 ± 1.3 (E1; 125 m), 17.0 ± 3.1 (E2; 35 m), to 19.9 ± 4.5 mmolC m^{-2} d^{-1} (E3; 50 m). The depth of this peak flux becomes notably shallower after E1. The epoch averaged flux values with standard deviation at the sample depths closest to the epoch averaged PPZ are as follows: 9.1 ± 1.1 (E1; PPZ = 67 m), 10.4 ± 2.3 (E2; PPZ = 90), and 14.2 ± 2.1 mmolC m^{-2} d^{-1} (E3; PPZ = 133 m).

The NEC group follows approximately the same temporal increase and magnitude of POC flux per epoch, with epoch averaged peak POC fluxes and standard deviations of approximately 12.1 ± NA (E1; 150 m), 17.4 ± 1.4 (E2; 225 m), and 18.3 ± 2.8 mmolC m^{-2} d^{-1} (E3; 225 m). The depth of the peak for E1 is approximately the same as in the EC group but becomes deeper in subsequent epochs, as opposed to shoaling observed in the EC group. The epoch averaged flux values and standard deviations at the sample depths closest to the epoch averaged PPZ are as follows: 6.2 ± NA (E1; PPZ = 53 m), 12.0 ± 1.6 (E2; PPZ = 94 m), and 16.6 ± 1.6 mmolC m^{-2} d^{-1} (E3; PPZ = 122 m). Data for all casts can be found in Supplemental Table 3.

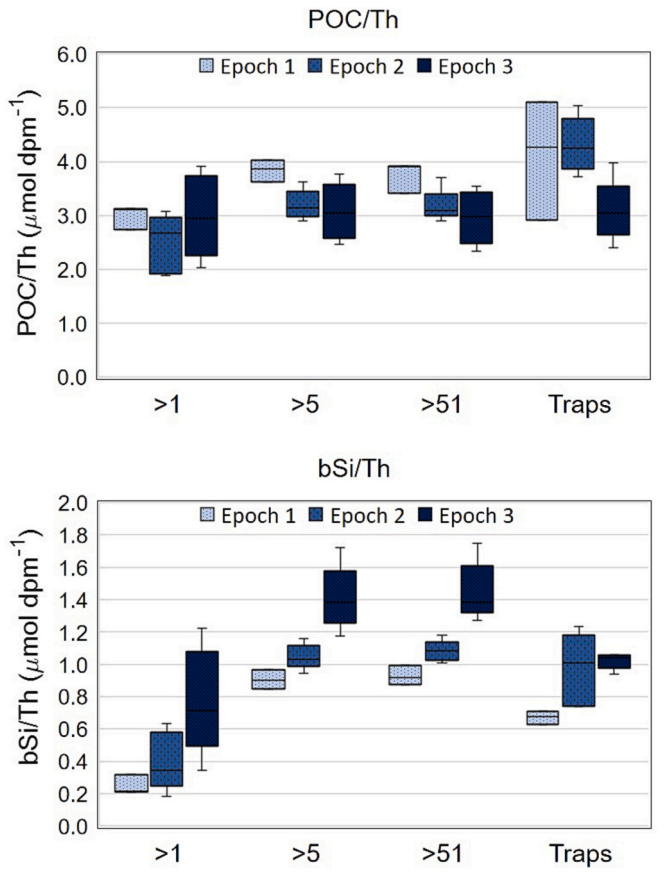

Fig. 4. Element/Th (particulate organic carbon, POC, and biogenic silica, bSi) ratios are presented here, showing variation of the 75–500 m depth range per epoch (colors, see legend) and sample size class (x-axis). Similarities between pump-collected size class (> 1, > 5, > 51 μm) compared to ratios from sediment traps were considered in order to make a decision on which size class is most representative of sinking particles. Whiskers represent the minimum and maximum, boxes represent the first and third quartile, and the line represents the median. Both POC/Th and bSi/Th ratios were considered in this decision, and ultimately the >5 μm size class was applied to determine both POC and bSi fluxes.

4.4. Biogenic silica flux results

Biogenic silica fluxes were calculated to help assess bloom characteristics, as it was known from various community composition analyses, sediment trap content, and nutrient analyses that diatoms were an important component of the bloom and related export fluxes.

Results from bSi flux analysis show a general trend of increasing flux throughout the cruise sampling period (Fig. 6, epoch average with standard deviation range). The maximum fluxes with standard deviation of the bSi epoch averages in the EC are as follows: 3.6 ± 0.4 (E1; 75 m), 4.3 ± 1.8 (E2; 410 m), and 7.2 ± 2.2 mmolbSi m^{-2} d^{-1} (E3; 500 m). The epoch averaged flux values at the sample depths closest to the epoch averaged PPZ are as follows: 3.6 ± 0.4 (E1; PPZ = 67 m), 3.4 ± 0.7 (E2; PPZ = 90 m), and 6.1 ± 0.9 mmolbSi m^{-2} d^{-1} (E3; PPZ = 133 m). Similarly, the maximum epoch averaged flux values with standard deviations for NEC are as follows: 3.2 ± NA (E1; 75 m), 5.7 ± 0.5 (E2; 225 m), and 7.9 ± 1.2 mmolbSi m^{-2} d^{-1} (E3; 225 m). At the epoch average PPZ in the NEC, flux values and standard deviations are: 2.6 ± NA (E1; PPZ = 53 m), 3.9 ± 0.5 (E2; PPZ = 94 m), and 7.1 ± 0.7 mmolbSi m^{-2} d^{-1} (E3; PPZ = 122 m). Epoch averaged data can be found in Table 4 (EC) and Supplemental Table 2 (NEC). Data for all casts can be found in Supplemental Table 3.

4.5. Biological carbon pump efficiency assessment

The Ez-ratio (defined in Section 3.4 as $Flux_{Ez}$/NPP), gives insight into the strength of the BCP. Depth-integrated NPP results with standard deviation are averaged over epoch and are as follows: 90 ± 10 (E1, n = 2), 82 ± 13 (E2, n = 4), 54 ± 9 mmolC m^{-2} d^{-1} (E3, n = 5), with all samples taken in the eddy center on the Process ship (J. Fox, personal communication; seen in Table 3). Results for Ez-ratio calculations using the PPZ show that the Ez-ratio increases from epoch to epoch regardless of the depth horizon considered, PPZ or 100 m, with the most significant change occurring between E2 and E3 (Fig. 7, Table 5). Results calculated using PPZ for the EC group show an approximate doubling of the Ez-ratio between epoch, and are as follows: 0.08 ± 0.01 (E1), 0.14 ± 0.03 (E2), and 0.26 ± 0.04 (E3). These results indicate that throughout the sampling period, the BCP becomes more efficient at exporting POC out of the PPZ. Considering NPP values and flux values, this increase in efficiency could be a function of both less NPP (decreasing values) and more export (increasing values), both driving greater export versus production over time. However, the Ez-ratio should be considered with caution, as the temporally variable Ez-ratios could also be reflective of a decoupling between export and production, which has been found to cause large variations in Ez-ratios (e.g., Wassmann, 1998; Henson et al., 2015).

Transfer efficiencies (T_{100}) are used to examine the extent of remineralization in the first 100 m below the Ez, where prior studies suggest that flux gradients and differences between sites can be large (e.g., Maiti et al., 2010). Transfer efficiencies were calculated using the specific PPZ of each cast, as well as using a fixed 100 m depth for comparison to other studies (Fig. 7, Table 5). The T_{100} calculated using PPZ depths in the EC group are as follows: 1.55 ± 0.35 (E1), 1.07 ± 0.15 (E2), and 1.07 ± 0.11 (E3). Had we used a 100 m depth to calculate T_{100}, results would be the same within uncertainty with the exception of E1, which is significantly lower (see Fig. 7, Table 5). Transfer efficiency values >1 are indicative of flux increases below the Ez, which could be due to in situ aggregation or repackaging processes occurring in the upper twilight zone, diel vertical migration and active transport injecting particles beneath the Ez, or a temporal lag of earlier higher fluxes (i.e., remnant high flux at depth is not related to low flux out of surface at the time of sampling). Regardless of the reason, the transfer of POC downwards once it reaches the PPZ is highly efficient and indicates limited impact of remineralization below the PPZ.

Considering these two metrics, Fig. 8 shows T_{100} (x-axis) against the Ez-ratio (y-axis), with contour lines showing overall BCP efficiency (i.e., the fraction of NPP that reaches a depth of 100 m below the Ez) and circle radii being proportional to the magnitude of NPP. This figure, first published in Buesseler and Boyd (2009), has been used in a number of subsequent studies (e.g., Siegel et al., 2016; Buesseler et al., 2020a; Siegel et al., 2021) to illustrate variations in BCP efficiencies across different regions and seasons. As observed in Fig. 8, in this study, the overall BCP efficiency varied between epochs, but generally not between the EC and NEC. In other words, E1 is characterized by ~10% of surface POC reaching the T_{100} boundary, increasing to ~13% in E2, and ~ 30% in E3. For the EC group in particular, the BCP efficiency change between E2 and E3 is driven by the Ez-ratio, possibly indicating a relatively more significant change in surface ecology versus ecology below the Ez. This temporal change highlights the importance of high-frequency, time-series style measurements during periods of dynamic system change such as a bloom scenario. Had the sampling period been shorter, the temporal evolution of BCP efficiency would not have been captured.

5. Discussion

5.1. Study and diatom bloom overview

The North Atlantic EXPORTS 2021 program was carried out with the goal of better elucidating links between the chemical and biological

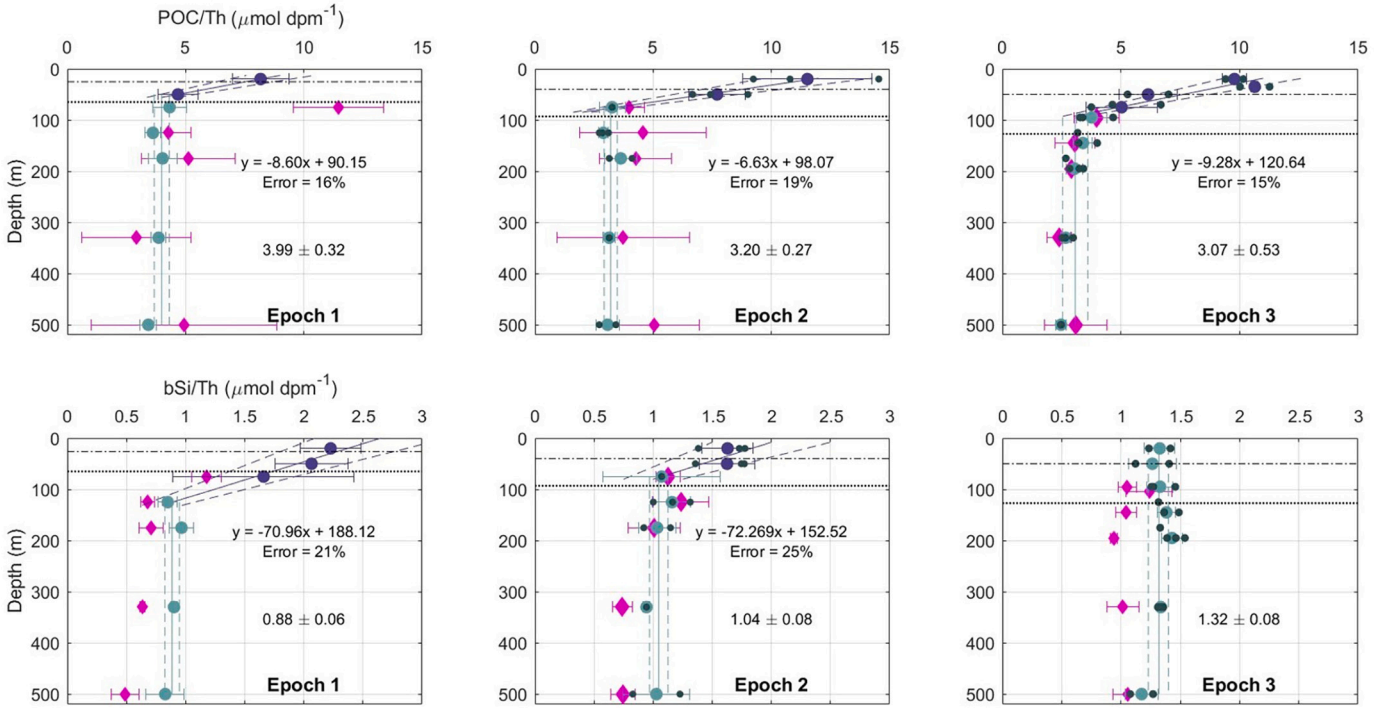

Fig. 5. POC/Th (top row) and bSi/Th ratios (bottom row) per epoch, as collected by McLane pumps and representative of the >5 μm particle size class, are shown here in μmol dpm^{-1}. Large symbols are representative of depth averages over all pump casts, while small symbols are individual data points. Dashed lines around the shallow depths linear fits are the average percent error range of the measurements, while dashed lines on deeper depths vertical fits are standard deviation of the individual measurements. Included for each epoch are the average PPZ (···) and MLD (– · -) depths for all casts in that epoch. Diamond symbols represent sediment trap data, included for general comparison.

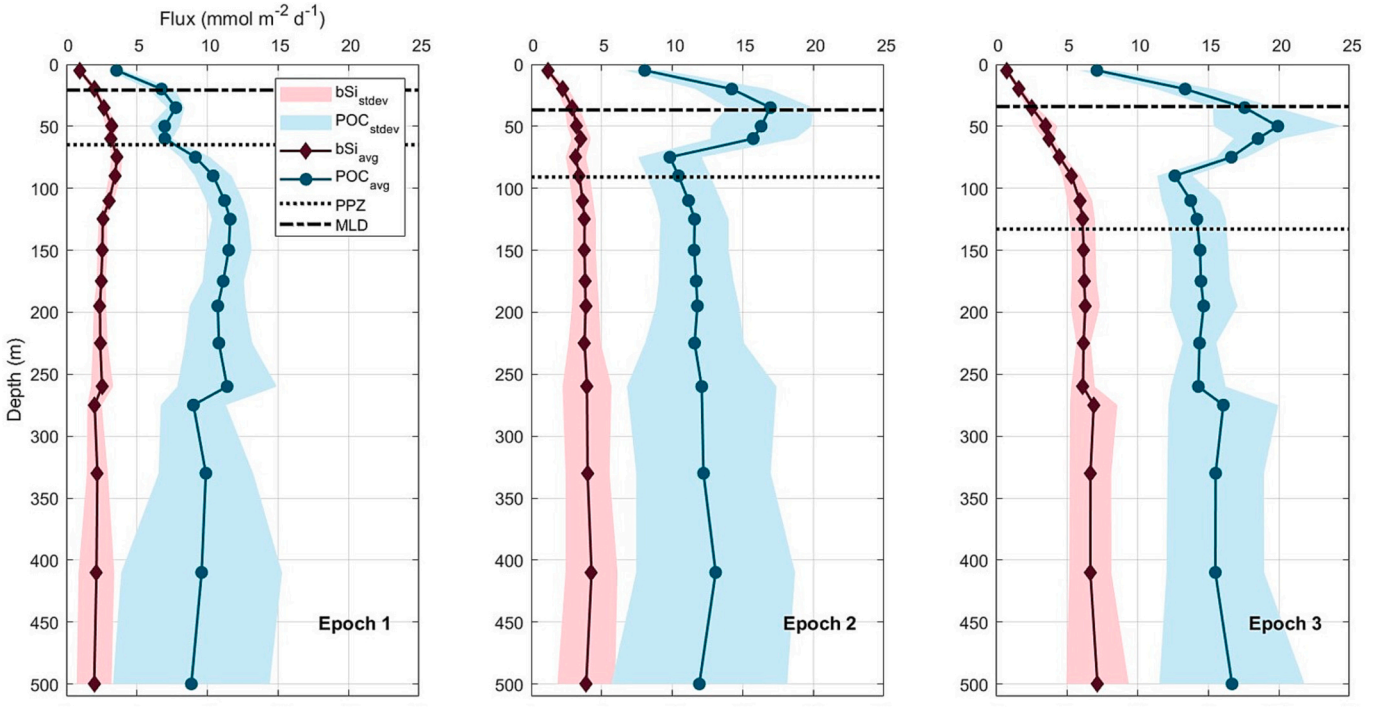

Fig. 6. Average flux profiles for biogenic silica (bSi, circles) and particulate organic carbon (POC, diamonds) from eddy center (EC) casts per epoch are presented, with shading indicating the standard deviation of the average. Horizontal lines show the epoch-average PPZ (dotted) and MLD (dashed) for corresponding casts. Evident here is the temporal evolution of fluxes of both species: bSi flux becomes more apparent in the mesopelagic (below the PPZ), and POC flux increases generally but particularly in the euphotic zone (above the PPZ).

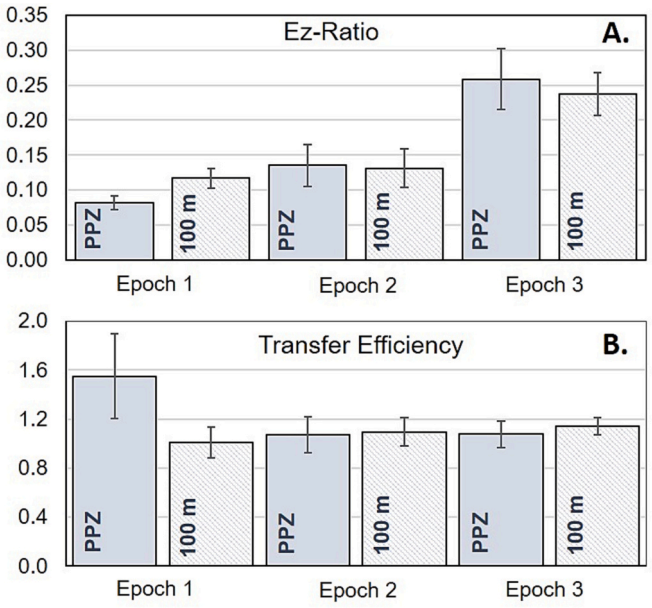

Fig. 7. Metrics classifying the biological carbon pump (BCP) are shown per epoch (x-axes). All flux data is particulate organic carbon (POC) flux, and for the eddy center (EC) group. Calculations on (A) and (B) are done using both PPZ and a standard 100 m as a proxy for Ez (see bar colour and labels). (A) shows Ez-ratio ($\frac{Flux_{Ez}}{NPP}$), classifying the strength of flux relative to production in the Ez; (B) shows transfer efficiency (T100; $\frac{Flux_{Ez+100}}{Flux_{Ez}}$) classifying flux attenuation below the Ez.

dynamics within an eddy during the demise of the spring bloom and the efficiency of carbon export and sequestration. Diatom blooms in the North Atlantic have been hypothesized to be initiated by deep winter mixing that dilutes predators and therefore decreases loss to grazing (Behrenfeld, 2010). The bloom accelerates as the mixed layer shoals in the spring and increased irradiance supports growth rates that continue to exceed predator grazing. These conditions combine to produce a system that quickly exhausts silica concentrations, leading to rapid changes in diatom growth rates, community structure and export (Gardner et al., 1993; Sieracki et al., 1993; Behrenfeld, 2010; Alkire et al., 2012). Export driven by diatoms has been described as "pulse-like" sedimentation events, and these contribute a large fraction of overall carbon export to the deep ocean (Lampitt, 1985; Smetacek, 1985; Berger and Wefer, 1990; Honjo and Manganini, 1993; Lampitt and Antia, 1997; Leblanc et al., 2005).

Prior studies in the North Atlantic that are critical to understanding export have shown that the amount of POC reaching depth is controlled heavily by diatom presence (Briggs et al., 2011; Rynearson et al., 2013; Le Moigne et al., 2014). Analysis of the system silica cycle and bSi flux is a natural complement to the carbon export dataset presented in this study, as it supports the hypothesis that the observed temporal carbon flux increase is indeed consistent with the demise of a diatom bloom. The sampling period began in a state of low silicic acid (dSi) concentration (< 1 μmol L^{-1}) and low Si/NO_3, indicating that substantial growth of diatoms had already occurred. Low dSi concentrations persisted through the cruise, but increased in response to storm-driven entrainment that replenished surface concentration to 1–2 μmol L^{-1}. However, despite increased available nutrient concentrations, surface bSi stocks continued to decline while mesopelagic bSi stocks increased – indicating diatom export through E2 and into E3 (M. Brzezinski, personal communication). These trends, along with overall decreasing NPP throughout the cruise, suggest that diatoms contributed to the observed trend of increasing POC flux over the sampling period, particularly into the mesopelagic.

5.2. Temporal evolution of carbon and biogenic silica fluxes

There is significant temporal evolution of the diatom bloom and its chemical and biological characteristics over the sampling period. Although there are slight differences in bSi and POC flux data between the EC and NEC groups (Table 4 and Supplemental Table 2), specifically as it relates to patterns with depth, we focus the following discussion on the EC flux data as eddy center casts are theoretically less influenced by physical transport than casts at the edge (Resplandy et al., 2012). Average EC flux profiles of POC and bSi are shown in Fig. 6 where two large patterns are particularly evident: (1) in E1, bSi fluxes above the PPZ are much closer in magnitude to POC fluxes than in the other epochs, and (2) while both cumulative POC and bSi fluxes ~100 m below the PPZ increase with time, the rate of increase is faster for bSi. In other words, bSi fluxes become comparatively closer to POC fluxes in E2 and E3 compared to in E1.

These features are further delineated by cast to cast temporal trends in bSi and POC fluxes at distinct depths, which reveal stark changes in bSi and POC export over time (Fig. 9). For POC (which encompasses diatom carbon + other carbon), there is a general increase in export over the sampling period at all depths. Biogenic silica flux similarly increases throughout the sampling period. However, these increases occur largely below the 50 m depth bin, lying below the mixed layer and close to the depth of the PPZ. The magnitude of the bSi fluxes relative to the POC

Table 5
Ez-ratio ($Flux_{Ez}$/NPP), and T_{100} ($Flux_{Ez+100m}/Flux_{Ez}$)for each epoch and group. Ez-ratios and T_{100} were calculated both using primary production zone (PPZ) and 100 m as the threshold for the Ez base. Epoch average standard deviations are included. Note that the Ez-ratio for the NEC is calculated using NPP from the EC. Therefore, this calculation is for general comparison purposes only.

Ez-Ratio									
PPZ					100 M				
	EC	(+/−)	NEC	(+/−)		EC	(+/−)	NEC	(+/−)
E1	0.08	0.01	0.06	NA	E1	0.12	0.01	0.11	NA
E2	0.14	0.03	0.15	0.03	E2	0.13	0.03	0.16	0.02
E3	0.26	0.04	0.29	0.05	E3	0.24	0.03	0.26	0.03
Universal Avg					*Universal Avg*				
	0.16	0.09				0.16	0.06		
T100									
PPZ					100 M				
	EC	(+/−)	NEC	(+/−)		EC	(+/−)	NEC	(+/−)
E1	1.55	0.35	2.18	NA	E1	1.01	0.12	1.08	NA
E2	1.07	0.15	1.31	0.17	E2	1.09	0.11	1.25	0.11
E3	1.07	0.11	1.16	0.11	E3	1.14	0.07	1.30	0.07
Universal Avg					*Universal Avg*				
	1.39	0.43				1.15	0.11		

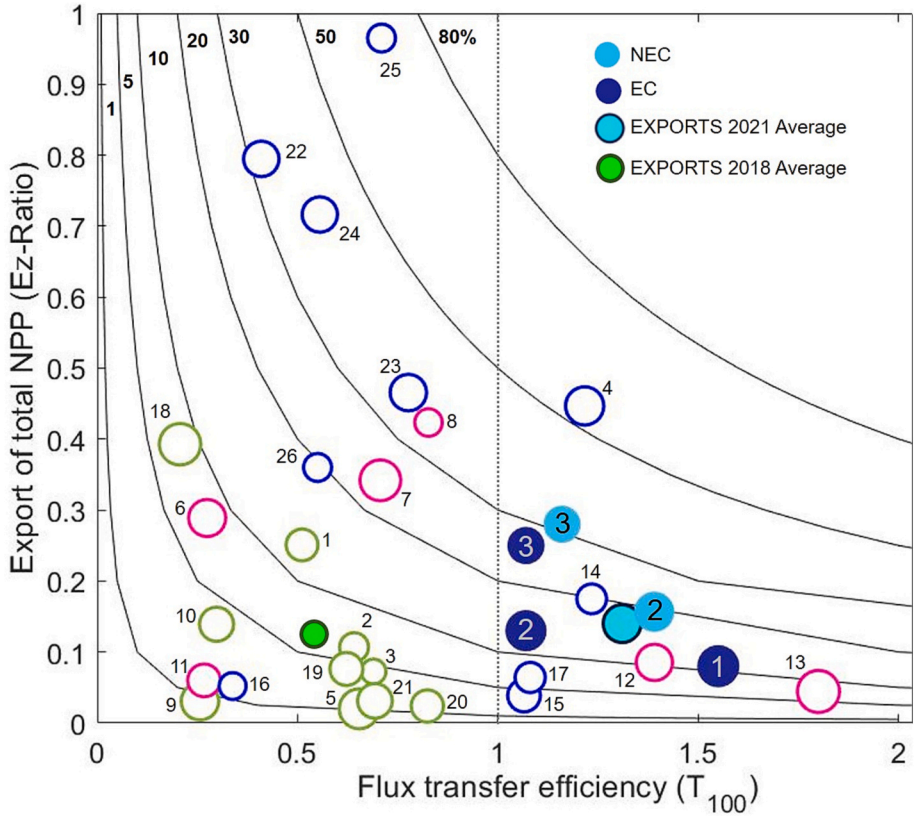

Fig. 8. Plot adapted from Buesseler and Boyd, 2009 and Buesseler et al. 2020, depicting transfer efficiency ($T_{100} = \frac{Flux_{Ez+100}}{Fluz_{Ez}}$) on the x-axis, and the export ratio (Ez-ratio $= \frac{Flux_{Ez}}{NPP}$) on the y-axis. Contour lines are overall BCP efficiency percentages, and symbol area is proportional to NPP. The filled bright green symbol corresponds to EXPORTS 2018 Ocean Station Papa (Buesseler et al. 2020). The filled blue symbols correspond to this study, as detailed in the legend, with 1–3 denoting epochs. Note that NEC data from E1 is omitted, as it was derived from one profile only. Open symbols are from previous studies (details corresponding to numbers in Supplemental Information), and are colour coded corresponding to region: North Atlantic Ocean (blue), Pacific Ocean (green), Southern Ocean (pink). (For interpretation of the references to colour in this figure legend, the reader is referred to the web version of this article.)

fluxes are shown as the average total bSi flux divided by POC flux ($\frac{Flux_{bSi}}{Flux_{POC}}$) per epoch, which is equivalent to the ratio of bSi to POC on >5 μm particles (Fig. 9, grey shaded area corresponding to third y-axis). The balance between silica production, bSi export and phytoplankton community structure is included in separate studies, and therefore the specific contribution of diatom carbon to the total carbon pool is not discussed further.

As both the numerator and denominator in the bSi/POC ratio changes, it is helpful to focus on temporal evolution of the ratio. The general stability of bSi flux compared to the increase in POC in the top 50 m of the water column causes the bSi/POC ratio to approximately halve from E1 to E2 in the 5–50 m depth bins: 0.26 to 0.15 (5 m), 0.29 to 0.16 (20 m), and 0.46 to 0.20 (50 m) (Fig. 8). This could indicate that after E1 diatom carbon contributes a decreasing portion of overall POC flux in the upper water column. However, in deeper waters (e.g. 150 m) the decreasing bSi/POC trend reverses to a temporal increase: 0.22 (E1), to 0.33 (E2), to 0.43 (E3). Presenting these numbers differently, the euphotic (5 m) and mesopelagic (150 m) ratios are approximately the same in E1 (0.26 vs. 0.22), double in E2 (0.15 vs. 0.33), and are four times higher in E3 (0.11 vs. 0.43) – showing an opposite temporal change in the flux composition between euphotic and mesopelagic depths over the sampling period. These trends could indicate that diatom flux contributes to an increasing portion of overall POC flux over time in deeper waters. In other words, both POC and bSi fluxes increase over time, but, particularly in the mesopelagic, bSi flux increases faster than POC flux.

Evaluation of the contribution of diatoms to POC flux considering bSi/POC ratios must account for the known trend of increasing bSi/POC ratio with depth as particles move through the water column. The efficiency of transport of bSi versus POC is driven largely by preferential remineralization of POC over bSi dissolution, along with other processes including herbivore grazing on diatoms within the mesopelagic (Nelson et al., 1995; Ragueneau et al., 2002; Thunell et al., 2008). The trends described above of increasing bSi/POC ratio in the mesopelagic over time could be simply from POC remineralization becoming comparatively more preferential than bSi dissolution over time. However, assuming that remineralization/dissolution of POC and bSi change roughly in parallel over time, the increase in the bSi/POC ratio in the mesopelagic throughout the sampling period temporally indicates a relative increase in the fraction of carbon carried to the mesopelagic zone by diatoms. This hypothesis parallels that derived from Marine Snow Catcher data (increasing bSi/POC ratio at depth over time; E. Romanelli, pers. communication). These patterns are consistent with a progressive increase in the contribution of diatoms to flux deeper in the water column during what appears to be the demise of a diatom bloom. Such changes occurring over a timescale of days to weeks contrast with diatom bloom termination via cell aggregation that often leads to an abrupt increase in diatom export, removing considerable biomass from surface waters and truncating quickly over the timescale of days (e.g., Billett et al., 1983; Thiel et al., 1989). While the observation presented here is specifically focused on termination and export, mixing caused by high winds in the North Atlantic during the spring (autumn observations are different) are known to slow down the development and progression of blooms by decreasing light-dependent mean specific growth rates of communities (Waniek, 2003; Ueyama and Monger, 2005; Henson et al., 2009; Rumyantseva et al., 2019). The system studied here was

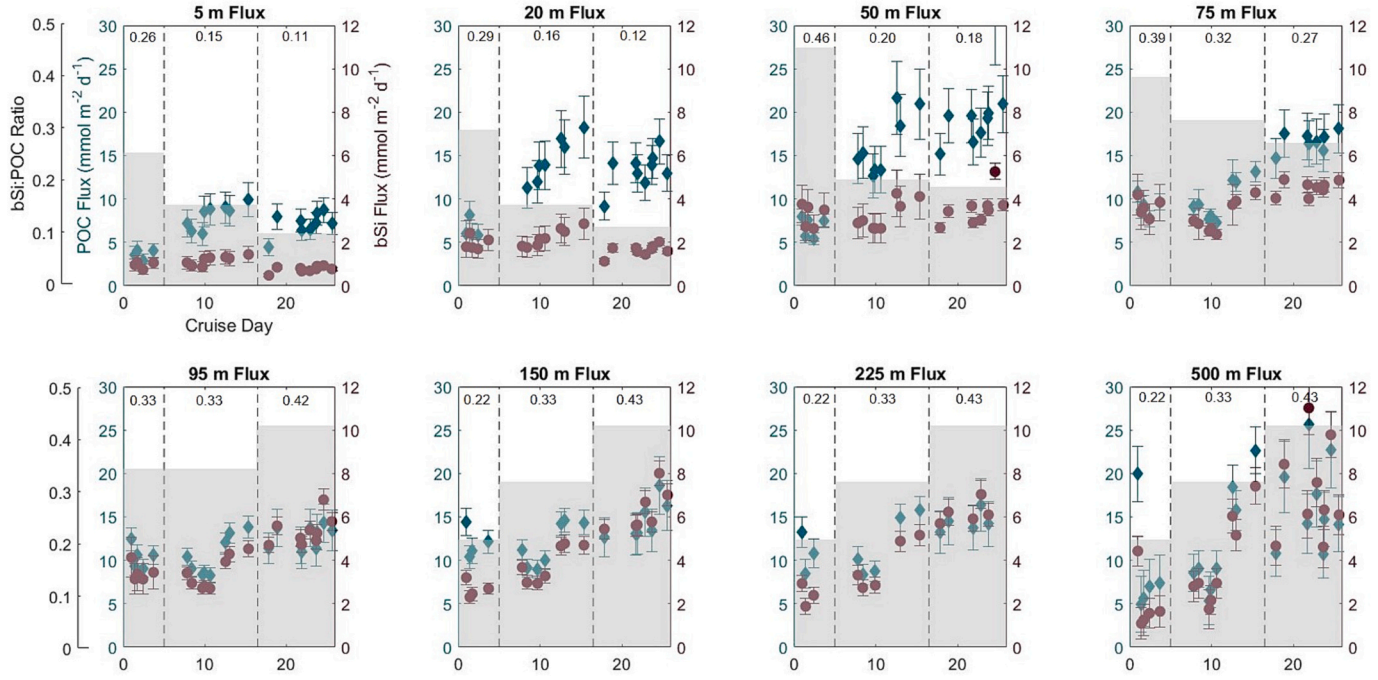

Fig. 9. Depth-specific temporal evolution of particulate organic carbon (POC, blue diamonds, left y-axis) and biogenic silica (bSi, red circles, right y-axis) flux values, over 5 to 500 m. Here, the temporal evolution of POC and bSi fluxes throughout the sampling period can be directly compared at 8 distinct depths. The third (black) y-axis represents the epoch average bSi/POC ratio. This is indicated on the plot with grey shading, and ratio values are written at the top of the plot for clarity. (For interpretation of the references to colour in this figure legend, the reader is referred to the web version of this article.)

interrupted by four storms encompassing 42% of the field program (Johnson et al., 2024). This could have simply resulted in slower biomass accumulation and thus bloom termination. Furthermore, storm-driven enhanced nutrient entrainment from surrounding waters (Johnson et al., 2024) could have also prolonged the bloom.

5.3. Comparison to similar studies in bloom systems

5.3.1. Studies in the North Atlantic

Biological carbon pump characteristics and POC export in the PAP area have long been a focus of study. During late April through May, Buesseler et al. (1992) applied a similar NSS ^{234}Th model to the one used here to estimate ^{234}Th uptake and removal rates, and ultimately POC export dynamics as part of the JGOFS program. In that study, they found that throughout the one-month occupation (only 4 casts) of the bloom progression, ^{234}Th export flux developed a "two-layered system" in which the mixed layer had POC export of 5–40 mmolC m^{-2} d^{-1}, with increased export continuing below the mixed layer, resulting in a $T_{100} >$ 1. Notably, the highest POC export values were found during the phase of the bloom where diatoms dominated the community structure, just before their demise (Buesseler et al., 1992). This is consistent with the data presented here, in which POC export peaks above the base of the euphotic zone, but then has a secondary increase in deeper waters. Similarly, the data consistently shows a T_{100} at or > 1, and a diatom-dominated community structure. Buesseler et al. (1992) also found an Ez-ratio of 0.05–0.42, consistent with results found in this study. A number of other studies in the North Atlantic region have found persistent export at depths deeper than the mixed layer, including the Iceland Basin (Martin et al., 2011), and PAP (Le Moigne et al., 2013; Ceballos-Romero et al., 2016) where disequilibria was present as deep as 400 m. The GEOTRACES cruise along the North Atlantic GA01 section (May–June) showed that surface POC export flux ranged from 1.4 mmolC m^{-2} d^{-1}, at stations where the bloom was close to its peak, to 12 mmolC m^{-2} d^{-1}, at stations where the bloom (with a mixed phytoplankton community with diatoms and coccolithophores) had already declined (Lemaitre et al., 2018). Similar POC export values were found on the same cruise derived from ^{210}Pb—^{210}Po disequilibrium (a longer integration time than the ^{234}Th method), ranging from negligible to 10 mmolC m^{-2} d^{-1}, with the highest fluxes and highest Ez-ratios found at sampling sites where diatoms were the dominant phytoplankton group (Tang et al., 2019).

Following a diatom bloom in the subpolar North Atlantic, Martin et al., 2011 measured downward POC flux following a Lagrangian float via the ^{234}Th disequilibrium method. They found that POC flux during the first three weeks of the diatom bloom was as low, < 1–2.5 mmolC m^{-2} d^{-1}, and rose to 30–50 mmolC m^{-2} d^{-1} in the top 100 m, 20 days after the bloom began. Data from co-occurrent sediment traps at 600 and 750 m suggested that 25–43% of the 100 m POC export sank below 750 m, indicating a strong BCP system. In a study at PAP that sampled in the summer (July–August) after a bloom that had been observed in May–June (Le Moigne et al., 2013), POC export fluxes derived using the ^{234}Th method were found to progress over time from 1.6 to 15 mmolC m^{-2} d^{-1} at 50 m and 1.7 to 17 mmolC m^{-2} d^{-1} at 150 m. This range, statistically the same between the 50 and 150 m depths, shows a system similar to this study, in that there is no significant POC export attenuation below the Ez. This study also measured bSi fluxes, ranging from 0.008 to 0.08 mmolbSi m^{-2} d^{-1} at 150 m, showing low post-bloom export (Le Moigne et al., 2013). Information on studies cited here can be found in Table 6. Overall, previous studies of diatom blooms in the North Atlantic show similar trends with respect to a temporal increase in POC export based on the presence and phase of the diatom bloom sampled.

5.3.2. Beyond the North Atlantic

The Southern Ocean is an area which presents an interesting counterpart to assessing BCP characteristics in a diatom bloom system. During the onset of a diatom-dominated bloom in the Kerguelen area of the Southern Ocean as part of the KEOPS2 study, POC export at 100 m varied from 3.5 to 11.8 mmolC m^{-2} d^{-1} over a 19-day sampling period (Planchon et al., 2015). This early-bloom flux was generally

Table 6
Comparison studies referred to in Discussion Section 5.3. Export ranges are POC export in mmolPOC m^{-2} d^{-1}.

Citation	Location	Time	Bloom Stage	POC Export	Depth
This Study	N. Atlantic (PAP)	May	Peak to demise	11 to 14	110 m
Buesseler et al., 1992	N. Atlantic (PAP)	April–May	Onset to peak	5 to 40	Mixed layer depth
Lemaitre et al., 2018	N. Atlantic (GEOVIDE track)	May–June	Onset to peak	1.4 to 12	Surface equilibrium depth
Martin et al., 2011	N. Atlantic (Iceland Basin)	May	Onset	1 to 2.5	100 m
Martin et al., 2011	N. Atlantic (Iceland Basin)	May	Onset to peak	30 to 50	100 m
Le Moigne et al., 2013	N. Atlantic (PAP)	July–August	Demise	1.6 to 15	50 m
Le Moigne et al., 2013	N. Atlantic (PAP)	July–August	Demise	1.7 to 17	150 m
Planchon et al., 2015	Southern Ocean (Kerguelen)	October–November	Onset	3.5 to 11.8	100 m
Savoye et al., 2008	Southern Ocean (Kerguelen)	January–February	Peak to demise	9 to 38	100 m
Roca-Martí et al., 2017	Southern Ocean (Atlantic)	January–March	Peak to demise	11 to 67	100 m
Buesseler et al., 2005	Southern Ocean	Artificial (SOFEX)	Onset	1 to 11	100 m

significantly lower than the KEOPS1 study that occurred at the peak and decline of a bloom in the same region. During the KEOPS1 study, POC fluxes at 100 m ranged from 9 to 38 mmolC m^{-2} d^{-1}, with export largely mediated by fast-sinking aggregates of silicified diatoms (Savoye et al., 2008). Following a vast diatom bloom during its decline in the Atlantic sector of the Southern Ocean, using ^{234}Th and sediment traps, Roca-Martí et al., 2017 showed high POC fluxes at 100 m (11 to 67 mmolC m^{-2} d^{-1}), but relatively low Ez-ratios compared to other diatoms blooms (< 0.2, Ez-ratios defined at 100 m). Taken together, these studies span different stages of a diatom bloom in the Southern Ocean, show POC fluxes that are generally low in the beginning of the bloom, and increase significantly at the peak and through the demise of the bloom. This is consistent with the study presented here, with a 30-day period of the demise of the bloom showing increasing POC flux driven by aggregates of sinking diatoms. Information on studies cited here can be found in Table 6.

The Southern Ocean Iron Fertilization Experiment (SOFeX) followed an artificial, iron fertilization-fueled bloom event, and offers an interesting comparison to this work (Buesseler et al., 2005). Both studies have T_{100} values consistently ≥ 1, resulting from continued increase in POC export beneath the base of the Ez (In Fig. 8, see numbers 11–13). The introduction of iron during the SOFeX study caused enhanced POC and bSi export out of the Ez as compared to a control outside of the study site, where POC export at 100 m in the study site from the beginning to the end of the sampling period ranged from 1 to 11 mmolC m^{-2} d^{-1}. Therein, iron addition in SOFeX created diatom bloom dynamics and resulting BCP characteristics that were similar to the North Atlantic bloom presented here. The induced diatom bloom at the point of sampling caused an increase in BCP efficiency of 1–10%, while the natural bloom presented here at the point of sampling shows an efficiency increase from 10 to 30%. However, the timeline of sampling between these two studies was different, which is reflected in study results: SOFeX sampled the initiation of the bloom while this study largely sampled the demise of the bloom. It would be a useful area of further study to follow the entire timeline of an artificial bloom with high-resolution ^{234}Th sampling. Regardless, these two, time series-style studies offer a comparison that can be informative in future iron addition and BCP enhancement experiments.

6. Conclusions

This study represents an important contribution not only to the literature assessing diatom blooms in the North Atlantic and in eddies, but also in the field's understanding of NSS systems and the ^{234}Th method application within them. A high spatial and temporal resolution ^{234}Th sampling scheme totaling 800 samples collected, in combination with POC and bSi/Th ratio determination on particles, allowed for the NSS derivation of POC and bSi fluxes throughout the upper 500 m of the water column. The unprecedented high resolution of this NSS study is unique in its scale, and both validates and expands on previous uses of an NSS model in ^{234}Th analysis.

Interrogation of differences between the temporal trends of bSi and POC fluxes is critical to understanding bloom dynamics and progression, thereby better understanding ocean carbon sequestration as a whole. Comparison of bSi and POC flux profiles, temporal trends, and bSi/POC ratios evidenced that bSi-driven flux out of the Ez into the mesopelagic increases over the sampling period, with a stronger increase for bSi than for POC. This indicates the progression of the demise of a diatom bloom. Further, this study suggests that the diatom export in the period of sampling occurred more gradually than many diatom bloom demise studies propose. Aggregation dynamics together with the ballasting effect of bSi fosters sinking of individual cells, and aggregates constitute a very efficient and robust biological carbon pump capable of sequestering carbon in the deep ocean. The more prolonged export of diatom standing stock observed in this sampling period may alter this dynamic, allowing more time for the remineralization of diatom POC relative to bSi possibly, and modulating the efficiency of diatom carbon export. Tracking fluxes of multiple elements with the ^{234}Th method gives extremely high-resolution direct comparison of species. This is critical for increased confidence in analysis of complex, dynamic environments.

During the sampling period, the overall efficiency of the BCP (as quantified by the amount of NPP reaching 100 m below the euphotic zone) increased from 10% in E1, to 13% in E2, and to 30% in E3. This observed tripling of BCP efficiency over a four-week sampling period is a case for high temporal resolution measurements tracking dynamic environments. Had the sampling period been shorter or shifted to another time period, an extremely different picture of the North Atlantic would have emerged. Thus, the analysis of the BCP as part of the global carbon cycle must be done through large scale sampling and observation schemes as conducted herein. Snapshots of systems fundamentally misrepresent the complexity of dynamic processes, and therefore skew science's view on the ocean's role in climate.

Funding

Authors would like to acknowledge support from the National Aeronautics and Space Administration (NASA) as part of the EXPORTS program awards 80NSSC17K0662, 80NSSC21K0015, 80NSSC17K0555; MRM was supported by funding from the Ocean Frontier Institute International Postdoctoral Fellowship Program and the Beatriu de Pinós Postdoctoral Program (2021-BP-00109); KOB and WB were supported by funding from the Woods Hole Oceanographic Institution's Ocean Twilight Zone study.

CRediT authorship contribution statement

Samantha J. Clevenger: Conceptualization, Data curation, Formal analysis, Investigation, Methodology, Visualization, Writing – original draft, Writing – review & editing. **Claudia R. Benitez-Nelson:** Conceptualization, Data curation, Funding acquisition, Project administration, Supervision, Writing – review & editing. **Montserrat Roca-Martí:** Data curation, Writing – original draft, Writing – review &

editing, Formal analysis. **Wokil Bam:** Data curation. **Margaret Estapa:** Data curation, Funding acquisition, Writing – review & editing. **Jennifer A. Kenyon:** Data curation. **Steven Pike:** Data curation. **Laure Resplandy:** Conceptualization, Funding acquisition, Supervision, Writing – review & editing. **Abigale Wyatt:** Formal analysis, Writing – original draft. **Ken O. Buesseler:** Conceptualization, Funding acquisition, Investigation, Supervision, Writing – review & editing, Project administration.

Declaration of Competing Interest

The authors have no competing interests.

Data availability

Data is available in NASA's SeaBASS repository

Acknowledgements

Thank you to Pat Kelly, Colleen Durkin, and Sean O'Neill for assistance with sediment trap data collection; to Jessica Drysdale for running PIC samples; to Gretchen Swarr for running the iCAP; to Ivona Cetinic, Dave Siegel, and the NASA EXPORTS Project Office for coordinating the EXPORTS efforts; thank you also to the captains and crews of the *RRS* James Cook and *RRS* Discovery. We also thank the three reviewers, including Frédéric Planchon and David DeMaster, for their generous donation of time that has resulted in an improved manuscript.

Appendix A. Supplementary data

Supplementary data to this article can be found online at https://doi.org/10.1016/j.marchem.2023.104346.

References

Alkire, M.B., D'Asaro, E., Lee, C., Perry, M.J., Gray, A., Cetinić, I., Briggs, N., Rehm, E., Kallin, E., Kaiser, J., González-Posada, A., 2012. Estimates of net community production and export using high-resolution Lagrangian measurements of O_2, NO_3^-, and POC through the evolution of a spring diatom bloom in the North Atlantic. Deep-Sea Res. I Oceanogr. Res. Pap. 64, 157–174.

Bacon, M.P., Anderson, R.F., 1982. Distribution of thorium isotopes between dissolved and particulate forms in the deep sea. J. Geophys. Res. 87, 2045–2056.

Bacon, M.P., Huh, C.-A., Fleer, A.P., Deuser, W.G., 1985. Seasonality in the flux of natural radionuclides and plutonium in the deep Sargasso Sea. Deep Sea Res. Part A 32, 273–286. https://doi.org/10.1016/0198-0149(85)90079-2.

Behrenfeld, M.J., 2010. Abandoning Sverdrup's critical depth hypothesis on phytoplankton blooms. Ecology 91, 977–989. https://doi.org/10.1890/09-1207.1.

Behrenfeld, M.J., Doney, S.C., Lima, I., Boss, E.S., Siegel, D.A., 2013. Annual cycles of ecological disturbance and recovery underlying the subarctic Atlantic spring plankton bloom. Global Biogeochem. Cycles. 27, 526–540.

Berger, W.H., Wefer, G., 1990. Export production: seasonality and intermittency, and palaeoceanographic implications. Palaeogeogr. Palaeoclimatol. Palaeoecol. 89, 245–254. https://doi.org/10.1016/0031-0182(90)90065-F.

Bhat, S.G., Krishnaswamy, S., Lal, D., Rama Moore, W.S., 1969. $^{234}Th/^{238}U$ ratios in the ocean. Earth Planet. Sci. Lett. 5, 483–491. https://doi.org/10.1016/S0012-821X(68)80083-4.

Billett, D.S.M., Lampitt, R.S., Rice, A.L., Mantoura, R.F.C., 1983. Seasonal sedimentation of phytoplankton to the deep-sea benthos. Nature 302, 520–522.

Binetti, U., Kaiser, J., Damarell, G.M., Rumyantseva, A., Martin, A.P., Henson, S., Heywood, K.J., 2020. Net community oxygen production derived from Seaglider deployments at the porcupine abyssal plain site (PAP; Northeast Atlantic) in 2012-13. Prog. Oceanogr. 183, 102293.

Bishop, J.K.B., Lam, P.J., Wood, T.J., 2012. Getting good particles: accurate sampling of particles by large volume in-situ filtration. Limnol. Oceanogr. Methods 10, 681–710. https://doi.org/10.4319/lom.2012.10.681.

Black, E.E., Lam, P.J., Lee, J.-M., Buesseler, K.O., 2018. Insights from the ^{238}U-^{234}Th method into the coupling of biological export and the cycling of cadmium, cobalt, and manganese in the Southeast Pacific Ocean. Global Biogeochem. Cycles 33, 15–36.

Black, E.E., Kienast, S.S., Lemaitre, N., Lam, P.J., Anderson, R.F., Planquette, H., Planchon, F., Buesseler, K.O., 2020. Ironing out Fe residence time in the dynamic upper ocean. Global Biogeochem. Cycles 34. https://doi.org/10.1029/2020GB006592.

Boyd, P.W., Claustre, H., Levy, M., Siegel, D.A., Weber, T., 2019. Multi-faceted particle pumps drive carbon sequestration in the ocean. Nature 568, 327–335. https://doi.org/10.1038/s41586-019-1098-2.

Briggs, N., Perry, M.J., Cetinić, I., Lee, C., D'Asaro, E., Gray, A.M., Rehm, E., 2011. High-resolution observations of aggregate flux during a sub-polar North Atlantic spring bloom. Deep-Sea Res. I Oceanogr. Res. Pap. 58, 1031–1039. https://doi.org/10.1016/j.dsr.2011.07.007.

Brown, O.B., Evans, R.H., Brown, J.W., Gordon, H.R., Smith, R.C., Baker, K.S., 1985. Phytoplankton blooming off the U.S. East Coast: A satellite description. Science 229, 163–167.

Brzezinski, M.A., Nelson, D.M., 1989. Seasonal changes in the silicon cycle within a Gulf Stream warm-core ring. Deep Sea Res. Part A 36, 1009–1030.

Buesseler, K.O., Boyd, P.W., 2009. Shedding light on the processes that control particle export and flux attenuation in the twilight zone of the open ocean. Limnol. Oceanogr. 54, 1210–1232.

Buesseler, K.O., Bacon, M.P., Cochran, J.K., Livingston, H.D., 1992. Carbon and nitrogen export during the JGOFS North Atlantic Bloom Experiment estimated from ^{234}Th:^{238}U disequilibria. Deep-Sea Res. I Oceanogr. Res. Pap. 39, 1115–1137.

Buesseler, K.O., Andrews, J.E., Pike, S.M., Charette, M.A., Goldson, L.E., Brzezinski, M. A., Lance, V.P., 2005. Particle export during the Southern Ocean Iron Experiment (SOFeX). Limnol. Oceanogr. 50, 311–327. https://doi.org/10.4319/lo.2005.50.1.0311.

Buesseler, K.O., et al., 2007. Revisiting carbon flux through the ocean's twilight zone. Science 316, 567–570.

Buesseler, K.O., Boyd, P.W., Black, E.E., Siegel, D.A., 2020a. Metrics that matter for assessing the ocean biological carbon pump. PNAS 117, 9679–9687. https://doi.org/10.1073/pnas.1918114117.

Buesseler, K.O., Benitez-Nelson, C.R., Roca-Martí, M., Wyatt, A.M., Resplandy, L., Clevenger, S.J., Drysdale, J.A., Estapa, M.L., Pike, S., Umhau, B.P., 2020b. High-resolution spatial and temporal measurements of particulate organic carbon flux using thorium-234 in the Northeast Pacific Ocean during the EXport processes in the ocean from RemoTe sensing field campaign. Elem. Sci. Anth. 8 https://doi.org/10.1525/elementa.2020.030.

Bury, S.J., Boyd, P.W., Preston, T., Savidge, G., Owens, N.J.P., 2001. Size-fractionated primary production and nitrogen uptake during a North Atlantic phytoplankton bloom: implications for carbon export estimates. Deep-Sea Res. I Oceanogr. Res. Pap. 48, 689–720. https://doi.org/10.1016/S0967-0637(00)00066-2.

Cavan, E.L., Le Moigne, F.A.C., Poulton, A.J., Tarling, G.A., Ward, P., Daniels, C.J., Fragoso, G.M., Sanders, R.J., 2015. Attenuation of particulate organic carbon flux in the Soctia Sea, Southern Ocean, is controlled by zooplankton fecal pellets. Geophys. Res. Lett. 42, 821–830. https://doi.org/10.1002/2014GL062744.

Ceballos-Romero, E., Le Moigne, F.A.C., Henson, S., Marsay, C.M., Sanders, R.J., García-Tenorio, R., Villa-Alfageme, M., 2016. Influence of bloom dynamics on particle export efficiency in the North Atlantic: a comparative study of radioanalytical techniques and sediment traps. Mar. Chem. 186, 198–210. https://doi.org/10.1016/j.marchem.2016.10.001.

Ceballos-Romero, E., De Soto, F., Le Moigne, F.A.C., García-Tenorio, R., Villa-Alfageme, M., 2018. ^{234}Th-derived particle fluxes and seasonal variability: when is the SS assumption reliable? Insights from a novel approach for carbon flux simulation. Geophys. Res. Lett. 45, 13414–13426. https://doi.org/10.1029/2018GL079968.

Clevenger, S.J., Benitez-Nelson, C.R., Drysdale, J., Pike, S., Puigcorbé, V., Buesseler, K. O., 2021. Review of the analysis of ^{234}Th in small volume (2-4L) seawater samples: improvements and recommendations. J. Radioanal. Nucl. Chem. 329, 1–13.

Coale, K.H., Bruland, K.W., 1987. Oceanic stratified euphotic zone as elucidated by ^{234}Th:^{238}U disequilibria. Limnol. Oceanogr. 32, 189–200.

Cochran, J.K., Masqué, P., 2003. Short-lived U/Th series radionuclides in the ocean: tracers for scavenging rates, export fluxes, and particle dynamics. Rev. Mineral. Geochem. 52, 461–492. https://doi.org/10.2113/0520461.

Cohn, M.R., Stephens, B., Meyer, M.G., Sharpe, G., Niebergall, A.K., Graff, J.R., Cassar, N., Marchetti, A., Carlson, C.A., Gifford, S., 2023. Microbial respiration in contrasting ocean provinces via high-frequency optical assays. preprint. https://doi.org/10.1101/2023.07.20.549894.

Cutter, G., Casciotti, K., Croot, P., Geibert, W., Heimbürger, L.-E., Lohan, M., Planquette, H., van de Flierdt, T., 2017. Sampling and Sample-handling Protocols for GEOTRACES Cruises. Version 3.0. https://doi.org/10.25607/OBP-2.

Dall'Olmo, G., Dingle, J., Polimene, L., Brewin, R.J.W., Claustre, H., 2016. Substantial energy input to the mesopelagic ecosystem from the seasonal mixed-layer pump. Nat. Geosci. 9, 820–823.

De La Rocha, C.L., Passow, U., 2007. Factors influencing the sinking of POC and the efficiency of the biological carbon pump. Deep-Sea Res. II Top. Stud. Oceanogr. 54, 639–658.

Erikson, Z.K., Fields, E., Omand, M.M., Johnson, L., Thompson, A.F., D'Asaro, E., Carvalho, F., Dove, L.A., Lee, C.M., Nicholson, D.P., Shilling, G., Cetinic, I., Siegel, D., 2022. EXPORTS North Atlantic Eddy tracking. NASA Technical Publication. (NASA/TM-20220009705).

Esaias, W.E., Feldman, G.C., McClain, C.R., Elrod, J.A., 1986. Monthly satellite-derived phytoplankton pigment distribution for the North Atlantic Ocean basin. EOS Trans. Am. Geo. Union 67, 835–837. https://doi.org/10.1029/EO067i044p00835.

Estapa, M.L., Durkin, C.A., Slade, W.H., Huffard, C.L., O'Neill, S.P., Omand, M.M., 2023. A new, global optical sediment trap calibration. Limnol. Oceanogr.: Methods.

Feely, R.A., Sabine, C.L., Takahashi, T., Wanninkhof, R., 2001. Uptake and storage of carbon dioxide in the ocean: the global CO_2 survey. Oceanography 14, 18–32.

Friedlingstein, P., O'Sullivan, M., Jones, M.W., et al., 2022. Global carbon budget 2022. Earth Syst. Sci. Data. 14, 4811–4900. https://doi.org/10.5194/essd-14-4811-2022.

Gardner, W.D., Walsh, I.D., Richardson, M.J., 1993. Biophysical forcing of particle production and distribution during a spring bloom in the North Atlantic. Deep-Sea Res. II Top. Stud. Oceanogr. 40, 171–195. https://doi.org/10.1016/0967-0645(93)90012-C.

Giering, S.L.C., et al., 2014. Reconciliation of the carbon budget in the ocean's twilight zone. Nature 507, 480–507. https://doi.org/10.1038/nature13123.

Gustafsson, Ö., Gschwend, P.M., Buesseler, K.O., 1997. Using ^{234}Th disequilibria to estimate the vertical removal rates of polycyclic aromatic hydrocarbons from the surface ocean. Mar. Chem. 57, 11–23.

Hartman, S.E., Bett, B.J., Durden, J.M., Henson, S.A., Iversen, M., Jeffreys, R.M., Horton, T., Lampitt, R., Gates, A.R., 2021. Enduring science: three decades of observing the Northeast Atlantic from the porcupine abyssal plain sustained observatory (PAP-SO). Prog. Oceanogr. 191, 102508 https://doi.org/10.1016/j.pocean.2020.102508.

Henson, S.A., Dunne, J.P., Sarmiento, J.L., 2009. Decadal variability in North Atlantic phytoplankton blooms. J. Geophys. Res. Oceans 114, C04013. https://doi.org/10.1029/2008JC005139.

Henson, S.A., Lampitt, R., Johns, D., 2012. Variability in phytoplankton community structure in response to the North Atlantic Oscillation and implications for organic carbon flux. Limnol. Oceanogr. 57, 1591–1601. https://doi.org/10.4319/lo.2012.57.6.1591.

Henson, S.A., Yool, A., Sanders, R., 2015. Variability in efficiency of particulate organic carbon export: a model study. Global Biogeochem. Cycles 29, 33–45. https://doi.org/10.1002/2014GB004965.

Henson, S., Le Moigne, F., Giering, S., 2019. Drivers of carbon export efficiency in the global ocean. Global Biogeochem. Cycles 33, 891–903. https://doi.org/10.1029/2018GB006158.

Honjo, S., Manganini, S.J., 1993. Annual biogenic particle fluxes to the interior of the North Atlantic Ocean; studied at 34°N 21°W and 48°N 21°W. Deep-Sea Res. II Top. Stud. Oceanogr. 40, 587–607. https://doi.org/10.1016/0967-0645(93)90034-K.

Honjo, S., Dymond, J., Collier, R., Manganini, S.J., 1995. Export production of particles to the interior of the equatorial Pacific Ocean during the 1992 EqPac experiment. Deep-Sea Res. II Top. Stud. Oceanogr. 42, 831–870. https://doi.org/10.1016/0967-0645(95)00034-N.

Huh, C.-A., Moore, W.S., Kadko, D.C., 1989. Oceanic ^{232}Th: a reconnaissance and implications of global distribution from manganese nodules. Geochim. Cosmochim. Acta 53, 1357–1366.

Huisman, J., van Oostveen, P., Weissing, F.J., 1999. Critical depth and critical turbulence: two different mechanisms for the development of phytoplankton blooms. Limnol. Oceanogr. 1781–1787.

Johnson, L., Siegel, D.A., Thompson, A.F., Fields, E., Erickson, Z.K., Cetinic, I., Lee, C.M., 2024. Assessment of oceanographic conditions during the North Atlantic EXport Processes in the Ocean from RemoTe Sensing (EXPORTS) field campaign. Prog. Oceanogr. 220, 103170.

Jónasdóttir, S.H., Visser, A.W., Richardson, K., Heath, M.R., 2015. Seasonal copepod lipid pump promotes carbon sequestration in the deep North Atlantic. Proc. Natl. Acad. Sci. U. S. A. 112, 12122–12126.

Kaufman, A., Li, Y.-H., Turekian, K.K., 1981. The removal rates of ^{234}Th and ^{228}Th from waters of the New York Bight. Earth Planet. Sci. Lett. 54, 385–392.

Kenyon, 2021. Anthropogenic and Natural Radioisotopes as Tracers for Contaminant Sources and Particulate Fluxes [Unpublished Doctoral Dissertation]. Massachusetts Institute of Technology and Woods Hole Oceanographic Institution.

Koski, M., Valencia, B., Newstead, R., Thiele, C., 2020. The missing piece of the upper mesopelagic carbon budget? Biomass, vertical distribution and feeding of aggregate-associated copepods at the PAP site. Prog. Oceanogr. 181, 102243.

Kwon, E.Y., Primeau, F., Sarmiento, J.L., 2009. The impact of remineralization depth on the air-sea carbon balance. Nat. Geosci. 2, 630–635.

Lacour, L., Briggs, N., Claustre, H., Ardyna, M., Dall'Olmo, G., 2019. The intraseasonal dynamics of the mixed layer pump in the subpolar North Atlantic Ocean: a biogeochemical-Argo float approach. Global Biogeochem. Cycles 33, 266–281. https://doi.org/10.1016/j.dsr.2013.09.005.

Lam, P.J., Ohnemus, D.C., Auro, M.E., 2015. Size-fractionated major particle composition and concentrations from the US GEOTRACES North Atlantic Zonal Transect. Deep Sea Res Part II Top Stud Oceanogr 116, 303–320. https://doi.org/10.1016/J.DSR2.2014.11.020.

Lamborg, C.H., Buesseler, K.O., Valdes, J., Bertrand, C.H., Bidigare, R., Manganini, S., Pike, S., Steinberg, D., Trull, T., Wilson, S., 2008. The flux of bio- and lithogenic material associated with sinking particles in the mesopelagic "twilight zone" of the northwest and north Central Pacific Ocean. Deep-Sea Res. II Top. Stud. Oceanogr. 55, 1540–1563. https://doi.org/10.1016/J.DSR2.2008.04.011.

Lampitt, R.S., 1985. Evidence for the seasonal deposition of detritus to the deep-sea floor and its subsequent resuspension. Deep Sea Res. Part A 32, 885–897. https://doi.org/10.1016/0198-0149(85)90034-2.

Lampitt, R.S., Antia, A.N., 1997. Particle flux in deep seas: regional characteristics and temporal variability. Deep-Sea Res. I Oceanogr. Res. Pap. 44, 1377–1403.

Langmuir, D., 1978. Uranium solution-mineral equilibria at low temperatures with applications to sedimentary ore deposits. Geochim. Cosmochim. Acta 42, 547–569. https://doi.org/10.1016/0016-7037(78)90001-7.

Le Moigne, F.A.C., Villa-Alfageme, M., Sanders, R.J., Marsay, C., Henson, S., García-Tenorio, R., 2013. Export of organic carbon and biominerals derived from ^{234}Th and ^{210}Po at the porcupine abyssal plain. Deep-Sea Res. I 72, 88–101.

Le Moigne, F.A.C., Pabortsava, K., Marcinko, C.L.J., Martin, P., Sanders, R.J., 2014. Where is mineral ballast important for surface export of particulate organic carbon in the ocean? Geophys. Res. Lett. 41, 8460–8468. https://doi.org/10.1002/2014GL061678.

Le Moigne, F.A.C., Poulton, A.J., Henson, S.A., Daniels, C.J., Fragoso, G.M., Mitchell, E., Richier, S., Russell, B.C., Smith, H.E.K., Tarling, G.A., Young, J.R., Zubkov, M., 2015. Carbon export efficiency and phytoplankton community composition in the Atlantic sector of the Arctic Ocean. J. Geophys. Res.: Oceans 120, 3896–3912. https://doi.org/10.1002/2015JC010700.

Le Moigne, F.A.C., Henson, S.A., Cavan, E., Georges, C., Pabortsava, K., Achterberg, E.P., Ceballos-Romero, E., 2016. What causes the inverse relationship between primary production and export efficiency in the Southern Ocean? Geophys. Res. Lett. 43, 4457–4466. https://doi.org/10.1002/2016GL068480.

Leblanc, K., Leynaert, A., Fernandez, C., Rimmelin, P., Moutin, T., Raimbault, P., Ras, J., Quéguiner, B., 2005. A seasonal study of diatom dynamics in the North Atlantic during the POMME experiment (2001): evidence for Si limitation of the spring bloom. J. Geophys. Res.: Oceans 110. https://doi.org/10.1029/2004JC002621.

Leblanc, K., Hare, C.E., Feng, Y., Berg, G.M., DiTullio, G.R., Neeley, A., Benner, I., Sprengel, C., Beck, A., Sanudo-Wilhelmy, S.A., Passow, U., Klinck, K., Rowe, J.M., Wilhelm, S.W., Brown, C.W., Hutchins, D.A., 2009. Distribution of calcifying and silicifying phytoplankton in relation to environmental and biogeochemical parameters during the late stages of the 2005 North East Atlantic spring bloom. Biogeosci. 6, 2155–2179.

Lemaitre, N., Planchon, F., Planquette, H., Dehairs, F., Fonseca-Batista, D., Roukaerts, A., Deman, F., Tang, Y., Mariez, C., Sarthou, G., 2018. High variability of particulate organic carbon export along the North Atlantic GEOTRACES section GA01 as deduced from ^{234}Th fluxes. Biogeosciences 15, 6417–6437. https://doi.org/10.5194/bg-15-6417-2018.

Lévy, M., et al., 2013. Physical pathways for carbon transfers between the surface mixed layer and the ocean interior. Global Biogeochem. Cycles 27, 1001–1012.

Li, Y.-H., Feely, H.W., Santschi, P.H., 1979. ^{228}Th:^{228}Ra radioactive disequilibrium in the New York bight and its implications for coastal pollution. Earth Planet. Sci. Lett. 42, 13–26.

Lochte, K., Ducklow, H.W., Fasham, M.J.R., Stienen, C., 1993. Plankton succession and carbon cycling at 47°N 20°W during the JGOFS North Atlantic bloom experiment. Deep-Sea Res. II Top. Stud. Oceanogr. 40, 91–114. https://doi.org/10.1016/0967-0645(93)90008-B.

Longhurst, A.R., 1991. Modelling the unpredictable. American Association for the Advancement of Science 242. Washington, DC.

Macovei, V.A., Hartman, S.E., Schuster, U., Torres-Valdés, S., Moore, C.M., Sanders, R.J., 2020. Impact of physical and biological processes on temporal variations of the ocean carbon sink in the mid-latitude North Atlantic (2002-2016). Prog. Oceanogr. 180.

Maier-Reimer, E., Mikolajewicz, U., Winguth, A., 1996. Future Ocean uptake of CO_2: interaction between ocean circulation and biology. Climate Dynam. 12, 711–722.

Maiti, K., Benitez-Nelson, C.R., Buesseler, K.O., 2010. Insights into particle formation and remineralization using the short-lived radionuclide, Thoruim-234. Geophys. Res. Lett. 37 https://doi.org/10.1029/2010GL044063.

Maiti, K., Buesseler, K.O., Pike, S.M., Benitez-Nelson, C.R., Cai, P., Chen, W., Cochran, K., Dai, M., Dehairs, F., Gasser, B., et al., 2012. Intercalibration studies of short-lived thorium-234 in the water column and marine particles. Limnol. Oceanogr. Methods 10, 631–644. https://doi.org/10.4319/lom.2012.10.631.

Marra, J.F., Lance, V.P., Vaillancourt, R.D., Hargreaves, B.R., 2014. Resolving the ocean's euphotic zone. Deep-Sea Res. I Oceanogr. Res. Pap. 83, 45–50. https://doi.org/10.1016/j.dsr.2013.09.005.

Martin, P., Lampitt, R.S., Perry, M.J., Sanders, R., Lee, C., D'Asaro, E., 2011. Export and mesopelagic particle flux during a North Atlantic spring diatom bloom. Deep-Sea Res. I Oceanogr. Res. Pap. 58, 338–349. https://doi.org/10.1016/j.dsr.2011.01.006.

McKinley, G.A., et al., 2016. Timescales for detection of trends in the ocean carbon sink. Nature 530, 469–472.

Meyer, M.G., Brzezinski, M.A., Cohn, M.R., Kramer, S.J., Paul, N., Sharpe, G., Niebergall, A.K., Gifford, S., Cassar, N., Marchetti, A., 2023. Primary production dynamics during the decline phase of the North Atlantic annual spring bloom. preprint. https://doi.org/10.1101/2023.05.18.541304.

Nelson, D.M., Tréguer, P., Brzezinski, M.A., Leynaert, A., Quéguiner, B., 1995. Production and dissolution of biogenic silica in the ocean: revised global estimates, comparison with regional data and relationship to biogenic sedimentation. Global Biogeochem. Cycles 9, 359–372. https://doi.org/10.1029/95GB01070.

Nozaki, Y., Yang, H.-S., Yamada, M., 1987. Scavenging of thorium in the ocean. J. Geophys. Res. 92, 772–778.

Omand, M.M., et al., 2015. Eddy-driven subduction exports particulate organic carbon from the spring bloom. Science 348, 222–225.

Owen, S.A., Buesseler, K.O., Sims, K.W.W., 2011. Re-evaluating the ^{238}U-salinity relationship in seawater: implications for the ^{238}U-^{234}Th disequilibrium method. Mar. Chem. 127, 31–39.

Owens, S.A., Pike, S., Buesseler, K.O., 2015. Thorium-234 as a tracer of particle dynamics and upper ocean export in the Atlantic Ocean. Deep-Sea Res. II Top. Stud. Oceanogr. 116, 42–59. https://doi.org/10.1016/j.dsr2.2014.11.010.

Parekh, P., Dutkiewicz, S., Follows, M.J., Ito, T., 2006. Atmospheric carbon dioxide in a less dusty world. Geophys. Res. Lett. 33 https://doi.org/10.1029/2005GL025098.

Pike, S., Buesseler, K.O., Andrews, J., Savoye, N., 2005. Quantification of the ^{234}Th recovery in small volume seawater samples by inductively coupled plasma mass spectrometry. J. Radioanal. Nucl. Chem. 263, 355–360.

Planchon, F., Ballas, D., Cavagna, A.-J., Bowie, A.R., Davies, D., Trull, T., Laurenceau-Cornec, E.C., Van Der Merwe, P., Dehairs, F., 2015. Carbon export in the naturally iron-fertilized Kerguelen area of the Southern Ocean based on the ^{234}Th approach. Biogeosciences 12, 3831–3848. https://doi.org/10.5194/bg-12-3831-2015.

Ragueneau, O., Dittert, N., Pondaven, P., Tréguer, P., Corrin, L., 2002. Si/C decoupling in the world ocean: is the Southern Ocean different? *Deep Sea res.* Part II 49, 3127–3154. https://doi.org/10.1016/S0967-0645(02)00075-9.

Resplandy, L., Martin, A.P., Le Moigne, F., Martin, P., Aquilina, A., Mémery, L., Lévy, M., Sanders, R., 2012. How does dynamical spatial variability impact 234Th-derived estimates of organic export? *Deep Sea res.* I 68, 24–45.
Resplandy, L., Lévy, M., McGillicuddy, D.J., 2019. Effects of eddy-driven subduction on ocean biological carbon pump. Global Biogeochem. Cycles 33, 1071–1084.
Riley, G.A., 1942. The relationship of vertical turbulence and spring diatom flowerings. J. Mar. Res. 5, 67–87.
Robertson, J.E., Watson, A.J., Langdon, C., Ling, R.D., Wood, J.W., 1993. Diurnal variation in surface pCO_2 and O_2 at 60°N, 20°W in the North Atlantic. Deep-Sea Res. II Top. Stud. Oceanogr. 40, 409–422. https://doi.org/10.1016/0967-0645(93)90024-H.
Roca-Martí, M., Puigcorbé, V., Iversen, M.H., Rutgers van der Loeff, M., Klaas, C., Cheah, W., Bracher, A., Masqué, P., 2017. High particulate organic carbon export during the decline of a vast diatom bloom in the Atlantic sector of the Southern Ocean. Deep-Sea Res. II Top. Stud. Oceanogr. 138, 102–115. https://doi.org/10.1016/j.dsr2.2015.12.007.
Roca-Martí, M., Benitez-Nelson, C.R., Umhau, B.P., Wyatt, A.M., Clevenger, S.J., Pike, S., Horner, T.J., Estapa, M.L., Resplandy, L., Buesseler, K.O., 2021. Concentrations, ratios, and sinking fluxes of major bioelements at Ocean Station papa. Elem. Sci. Anth. 9, 00166. https://doi.org/10.1525/elementa.2020.00166.
Rumyantseva, A., Henson, S., Martin, A., Thompson, A.F., Damarell, G.M., Kaiser, J., Heywood, K.J., 2019. Phytoplankton spring bloom initiation: the impact of atmospheric forcing and light in the temperate North Atlantic Ocean. Prog. Oceanogr. 178, 102202.
Rynearson, T.A., Richardson, K., Lampitt, R.S., Sieracki, M.E., Poulton, A.J., Lyngsgaard, M.M., Perry, M.J., 2013. Major contribution of diatom resting spores to vertical flux in the sub-polar North Atlantic. Deep-Sea Res. I Oceanogr. Res. Pap. 82, 60–71. https://doi.org/10.1016/j.dsr.2013.07.013.
Sanders, R., Henson, S.A., Koski, M., Rocha, C.L.D.L., Painter, S.C., Poulton, A.J., Riley, J., Salihoglu, B., Visser, A., Yool, A., Bellerby, R., Martin, A., 2014. The biological carbon pump in the North Atlantic. Prog. Oceanogr. 129, 200–218. https://doi.org/10.1016/j.pocean.2014.05.005.
Santschi, P.H., Murray, J.W., Baskaran, M., Benitez-Nelson, C.R., Guo, L.D., Hung, C.-C., Lamborg, C., Moran, S.B., Passow, U., Roy-Barman, M., 2006. Thorium speciation in seawater. Mar. Chem. 100, 250–268.
Sarmiento, J.L., Gruber, N., 2006. Ocean Biogeochemical Dynamics Ch, vol. 8. Princeton Univ. Press, Princeton.
Sarmiento, J.L., Toggweiler, J.R., 1984. A new model for the role of the oceans in determining atmospheric PCO_2. Nature 308, 621–624.
Savidge, G., Boyd, P., Pomroy, A., Harbour, D., Joint, I., 1995. Phytoplankton production and biomass estimates in the Northeast Atlantic Ocean, may-June 1990. Deep-Sea Res. I Oceanogr. Res. Pap. 42, 599–617. https://doi.org/10.1016/0967-0637(95)00016-Y.
Savoye, N., Benitez-Nelson, C.R., Burd, A.B., Cochran, J.K., Charette, M., Buesseler, K.O., Jackson, G.A., Roy-Barman, M., Schmidt, S., Elskens, M., 2006. ^{234}Th sorption and export models in the water column: a review. Mar. Chem. 100, 234–249.
Savoye, N., Trull, T.W., Jacquet, S.H.M., Navez, J., Dehairs, F., 2008. ^{234}Th-based export fluxes during a natural iron fertilization experiment in the Southern Ocean (KEOPS). Deep-Sea Res. II Top. Stud. Oceanogr. 55, 841–855. https://doi.org/10.1016/j.dsr2.2007.12.036.
Siegel, D.A., Buesseler, K.O., Behrenfeld, M.J., Benitez-Nelson, C.R., Boss, E., Brzezinski, M.A., Burd, A., Carlson, C.A., D'Asaro, E.A., Doney, S.C., Perry, M.J., Stanley, R.H.R., Steinberg, D.K., 2016. Prediction of the export and fate of global ocean net primary production: the EXPORTS science plan. Front. Mar. Sci. 3 https://doi.org/10.3389/fmars.2016.00022.
Siegel, D.A., et al., 2021. An operational overview of the EXport Processes in the Ocean from RemoTe sensing (EXPORTS) Northeast Pacific field deployment. Elem. Sci. Anth. 9 https://doi.org/10.1525/elementa.2020.00107.
Sieracki, M.E., Verity, P.G., Stoecker, D.K., 1993. Plankton community response to sequential silicate and nitrate depletion during the 1989 North Atlantic spring bloom. Deep-Sea Res. II Top. Stud. Oceanogr. 40, 213–225. https://doi.org/10.1016/0967-0645(93)90014-E.
Smetacek, V.S., 1985. Role of sinking in diatom life-history cycles: ecological, evolutionary and geological significance. Mar. Biol. 84, 239–251.
Smythe-Wright, D., Boswell, S., Kim, Y.-N., Kemp, A., 2010. Spatio-temporal changes in the distribution of phytopigments and phytoplanktonic groups at the porcupine abyssal plain (PAP) site. Deep-Sea Res. II Top. Stud. Oceanogr. 57, 1324–1335.
Stukel, M.R., Song, H., Goericke, R., Miller, A.J., 2017. The role of subduction and gravitational sinking in particle export, carbon sequestration, and the remineralization length scale in the California current ecosystem. Limnol. Oceanogr. 63, 363–383.
Sundby, S., Drinkwater, K.F., Kjesbu, O.S., 2016. The North Atlantic spring-bloom system – where the changing climate meets the winter dark. Front. Mar. Sci. 3, 28. https://doi.org/10.3389/fmars.2016.00028.
Sverdrup, H.U., 1953. On conditions for the vernal blooming of phytoplankton. ICES J. Mar. Sci. 18, 287–295. https://doi.org/10.1093/icesjms/18.3.287.
Tang, Y., Lemaitre, N., Castrillejo, M., Roca-Martí, M., Masqué, P., Stewart, G., 2019. The export flux of particulate organic carbon derived from ^{210}Po/^{210}Pb disequilibria along the North Atlantic GEOTRACES GA01 transect: GEOVIDE cruise. Biogeosciences 16, 309–327. https://doi.org/10.5194/bg-16-309-2019.
Tesán Onrubia, J.A., Petrova, M.V., Puigcorbé, V., Black, E.E., Valk, O., Dufour, A., Hamelin, B., Buesseler, K.O., Masqué, P., Le Moigne, F.A.C., Sonke, J.E., Rutgers van der Loeff, M., Heimbürger-Boavida, L.-E., 2020. Mercury export flux in thr Arctic Ocean estimated from ^{234}Th/^{238}U disequilibria. ACS Earth Space Chem. 4, 795–801. https://doi.org/10.1021/acsearthspacechem.0c00055.
Thiel, H., et al., 1989. Phytodetritus on the deep-sea floor in a central oceanic region of the Northeast Atlantic. Biol. Oceanogr. 6, 203–239.
Thunell, R., Benitez-Nelson, C.R., Muller-Karger, F., Lorenzoni, L., Fanning, K., Scranton, M., Varela, R., Astor, Y., 2008. Si cycle in the Cariaco Basin, Venezuela: Seasonal variability in silicate availability and the Si:C:N composition of sinking particles. Global Biogeochem. Cycles 22. https://doi.org/10.1029/2007GB003096.
Ueyama, R., Monger, B.C., 2005. Wind-induced modulation of seasonal phytoplankton blooms in the North Atlantic derived from satellite observations. Limnol. Oceanogr. 50, 1820–1829.
Verdeny, E., Masqué, P., Garcia-Orellana, J., Hanfland, C., Cochran, J.K., Stewart, G.M., 2009. POC export from ocean surface waters by means of ^{234}Th/^{238}U and ^{210}Po/^{210}Pb disequilibria: a review of the use of two radiotracer pairs. Deep Sea Res. 56, 1502–1518.
Volk, T., Hoffert, M., 1985. In: Sundquist, E.T., Broecker, W.S. (Eds.), In the Carbon Cycle and Atmospheric CO_2: Natural Variations Archean to Present, vol. 32. American Geophysical Union, Washington, DC, pp. 99–110.
Waniek, J.J., 2003. The role of physical forcing in initiation of spring blooms in the Northeast Atlantic. J. Mar. Syst. 39, 57–82.
Wassmann, P., 1998. Retention versus export food chains: processes controlling sinking loss from marine pelagic systems. Hydrobiologia 363, 29–57.
Weinstein, S.E., Moran, S.B., 2005. Vertical flux of particulate Al, Fe, Pb, and Ba from the upper ocean estimated from ^{234}Th/^{238}U disequilibria. Deep-Sea Res. I Oceanogr. Res. Pap. 52, 1477–1488. https://doi.org/10.1016/j.dsr.2005.03.008.